THE ASTROPHYSICAL JOURNAL, 563:694–715, 2001 December 20

THE URSA MAJOR CLUSTER OF GALAXIES. V. H I ROTATION CURVE SHAPES AND THE TULLY-FISHER RELATIONS

MARC A. W. VERHEIJEN
Department of Astronomy, University of Wisconsin, 475 North Charter Street, Madison, WI 53706; verheyen@astro.wisc.edu
Received 2001 May 25; accepted 2001 August 16

ABSTRACT

This paper investigates the statistical properties of the Tully-Fisher (TF) relations for a volume-limited complete sample of spiral galaxies in the nearby Ursa Major Cluster. The merits of B, R, I, and K' surface photometry and the availability of detailed kinematic information from H I synthesis imaging have been exploited. In addition to the corrected H I global profile widths $W^i_{R,I}$, the available H I rotation curves allow direct measurements of the observed maximum rotational velocities $V_{\rm max}$ and the amplitudes $V_{\rm flat}$ of the outer flat parts. The dynamical state of the gas disks could also be determined in detail from the radio observations. The four luminosity and three kinematic measures allowed the construction of 12 correlations for various subsamples. For large galaxy samples, the $M^{b,i}_R$–log $W^i_{R,I}$ correlation in conjunction with strict selection criteria is preferred for distance determinations with a 7% accuracy. Galaxies with rotation curves that are still rising at the last measured point lie systematically on the low-velocity side of the TF relation. Galaxies with a partly declining rotation curve ($V_{\rm max} > V_{\rm flat}$) tend to lie systematically on the high-velocity side of the relation when using $W^i_{R,I}$ or $V_{\rm max}$. However, systematic offsets are eliminated when $V_{\rm flat}$ is used. Residuals of the $M^{b,i}_B$–log $(2V_{\rm flat})$ relation correlate consistently with global galaxy properties along the Hubble sequence like morphological type, color, surface brightness, and gas mass fraction. These correlations are absent for the near-infrared $M^{b,i}_{K'}$–log $(2V_{\rm flat})$ residuals. The tightest correlation ($\chi^2_{\rm red} = 1.1$) is found for the $M^{b,i}_{K'}$–log $(2V_{\rm flat})$ relation, which has a slope of -11.3 ± 0.5 and a total observed scatter of 0.26 mag with a most likely intrinsic scatter of zero. The tightness of the near-infrared correlation is preserved when converting it into a baryonic TF relation that has a slope of -10.0 in the case $(\mathscr{M}_{\rm gas}/L_{K'}) = 1.6$ while a zero intrinsic scatter remains most likely. Based on the tightness of the near-infrared and baryonic correlations, it is concluded that the TF relation reflects a fundamental correlation between the mass of the dark matter halo, measured through its induced maximum rotational velocity $V_{\rm flat}$, and the total baryonic mass $\mathscr{M}_{\rm bar}$ of a galaxy where $\mathscr{M}_{\rm bar} \propto V^4_{\rm flat}$. Although the actual distribution of the baryonic matter inside halos of similar mass can vary significantly, it does not affect this relation.

Subject headings: dark matter — galaxies: clusters: individual (Ursa Major) — galaxies: fundamental parameters — galaxies: kinematics and dynamics — galaxies: spiral — galaxies: structure

On-line material: machine-readable table

1. INTRODUCTION

Numerous studies of the Tully-Fisher (TF) relations and their applications have been conducted in the past. In most cases their aim was to find observables that reduce the scatter and thus improve this relation as a tool for measuring distances to spiral galaxies (e.g., Peletier & Willner 1993; Giovanelli et al. 1997). However, the statistical properties of the TF relation are also used to constrain numerical simulations of galaxy formation (e.g., Navarro & Steinmetz 2000; Bullock et al. 2001), to probe galaxy evolution on cosmological timescales (e.g., Vogt et al. 1997; Rix et al. 1997), to determine mass-to-light ratios of the stellar populations (e.g., Bell & de Jong 2001), and to gain insights in the formation and structure of galaxies (e.g., Courteau & Rix 1999; Hinz, Rix, & Bernstein 2001).

The rapid development of optical and near-infrared detector arrays has led to greatly improved measurements of the luminosities of spiral galaxies, ranging from the originally estimated photographic B magnitudes (Tully & Fisher 1977) to the present high-quality near-infrared surface photometry (e.g., Peletier & Willner 1993; Tully et al. 1996, hereafter Paper I; Malhotra et al. 1996). The main advantages of near-infrared luminosities are that stellar mass-to-light ratios are less affected by population differences and that extinction corrections are minimal. However, various studies yield conflicting results as far as the scatter in the near-infrared relations is concerned. For example, for a sample of Ursa Major (UMa) spirals, Pierce & Tully (1988) found total scatters of 0.28 and 0.31 mag by using I and $H_{-0.5}$ magnitudes, respectively. Bernstein, Guhathakurta, & Raychaudhury (1996), using 23 spirals in Coma, also found that the H-band TF relation has no less scatter than the I-band relation. On the other hand, Malhotra et al. (1996) report scatters as low as 0.09, 0.13, and 0.20 mag for the J, K, and L passbands, respectively, using DIRBE maps for a sample of nearby galaxies with Cepheid distances.

It is important to realize, however, that results from various independent studies cannot simply be compared at face value because of different sample sizes and selection criteria, photometric passbands, correction algorithms, fitting methods, and statistical techniques. For instance, the sample of Malhotra et al. (1996) consists of only seven galaxies, and such small samples are known to yield artificially low rms scatters when a least-squares fitting method is applied (e.g., Freedman 1990). For cluster samples, the rms

scatter will be systematically larger as a result of the depth and velocity dispersion of the cluster. As an extreme example, Kraan-Korteweg, Cameron, & Tammann (1988) reported a scatter of 0.77 mag in the blue TF relation for a sample of 127 galaxies in the Virgo Cluster, and it was shown by Pierce & Tully (1988) that this large scatter was caused by contamination of foreground and background galaxies that could not be identified and removed as a result of the cluster's large velocity dispersion. Two recent studies, one by Sakai et al. (2000) and one by Tully & Pierce (2000), used nearly identical samples of nearby galaxies with independent measured Cepheid distances, and both studies included *B*-, *R*-, and *I*-band photometry. Nevertheless, systematically different results were reported in the sense that Tully & Pierce (2000) found shallower slopes, smaller scatters, and brighter zero points than Sakai et al. (2000) did, for each of those three passbands. These differences can be largely attributed to different extinction and other corrections. Furthermore, from a statistical point of view, it should be noted that the scatter is closely related to the slope of the relation; a steeper slope gives a larger scatter for the same uncertainties in the observables.

Most of the above-mentioned studies made use of the width $W^i_{R,I}$ of global H I profiles, corrected for instrumental resolution (*R*), internal turbulent motion (*I*), and the inclination of the *stellar* disk (*i*). Although it is widely recognized that the width of the H I profile is related to a galaxy's rotation, relatively little attention has been given to what this H I line width actually conveys. To some approximation, the rotational velocity of a spiral galaxy might be derived from the properly corrected width of its global H I profile. Indeed, this might be the case if the rotation curve of the H I disk rises monotonically in the inner regions and levels off to a constant velocity $V_{\rm flat}$ in the flat extended outer parts, yielding the characteristic double-horned global profile. However, the width and detailed shape of a global H I profile is determined by the shape of a galaxy's rotation curve, the distribution of the H I gas in the disk, and the possible presence of a warp or noncircular motion.

From H I synthesis mapping of spirals it has become clear that there are two basic deviations from this classical rotation curve shape. First, many low surface brightness (LSB) and dwarf galaxies only show the rising part of the rotation curve; their H I disks do not extend far enough to probe the regime of constant rotational velocity in the halo. Consequently, their observed maximum rotational velocity $V_{\rm max}$ provides merely a lower limit to the actual rotational velocity induced by the potential of their dark matter halo. Second, the more massive and compact galaxies often show a steep rise of the rotation curve, which reaches a maximum $V_{\rm max}$ in the optical region followed by a modest decline until $V_{\rm flat}$ is reached in the outer flat parts (e.g., Casertano & van Gorkom 1991). In this case $V_{\rm max}$ exceeds $V_{\rm flat}$. The study presented in this paper aims at understanding the statistical properties of the $W^i_{R,I}$-based TF relation (tightness, scatter, and slope) using knowledge of these detailed shapes of the H I rotation curves and the characteristics of the full galaxy velocity fields. Furthermore, it investigates whether such detailed kinematic information can be used to improve the TF relation as a distance estimator and whether it is helpful in gaining a better understanding of its physical basis.

The outline of this paper is as follows. Section 2 describes the selected galaxy sample. Section 3 provides details on the available data. Section 4 explains the different shapes of the H I rotation curves that can be identified. In § 5 various subsamples are defined on the basis of the availability and characteristics of the kinematic data. Section 6 gives some special attention to the corrections for internal extinction. Section 7 describes the constructed TF relations using the luminosities measured in the *B*, *R*, *I*, and *K'* passbands and the various kinematic measures $W^i_{R,I}$, $V_{\rm max}$, and $V_{\rm flat}$. The fitting method will be explained and the statistical properties of the TF relations will be examined given the shapes of the rotation curves. The residuals are examined in § 8 in search of a possible second parameter. Section 9 discusses the magnitude of any intrinsic scatter required to explain the total observed scatter. In § 10 the issue of the LSB galaxies and their location on the TF relation is briefly discussed. Section 11 explores the properties of the baryonic TF relation. In § 12 the results are discussed in relation to other studies that consider the shapes of rotation curves. An attempt is made to identify the fundamental parameters of a galaxy that form the physical basis of the TF correlation. Finally, § 13 gives a summary of this paper.

2. THE SAMPLE

The spiral-rich and dynamically quiescent UMa Cluster was selected for the present study. An extensive description of this cluster is given in Paper I. Paper I also contains the photometric data and high-quality blue and near-infrared images of all the cluster members. The H I synthesis imaging data of UMa Cluster galaxies relevant for this TF study are presented by Verheijen & Sancisi (2001, hereafter Paper IV). Tully & Verheijen (1997, hereafter Paper II) investigate the optical and near-infrared central disk surface brightness distributions, and the high surface brightness (HSB) and LSB galaxies in the UMa Cluster are identified in this paper. For completeness, Trentham, Tully, & Verheijen (2001, hereafter Paper III) deal with the faint end of the *R*-band luminosity function in the UMa Cluster.

Several characteristics of the UMa sample have been updated since Paper I was published. First of all, using newly available Cepheid distances to local TF calibrator galaxies (e.g., Sakai et al. 2000), the distance to the UMa Cluster was revised from 15.5 Mpc in Paper I to 18.6 Mpc (Tully & Pierce 2000), which is the distance adopted in this paper. This new distance was also used in Papers III and IV. Second, new corrections for internal extinction have been derived by Tully et al. (1998) based on a $\gamma \log (b/a)$ scheme instead of the Tully & Fouqué (1985, hereafter TF85) method that was used in Paper I. The differences between these correction methods and their consequences will be addressed later in this paper. Third, the CfA2 redshift catalog has a deeper completion limit of $m_z = 15.5$ instead of the CfA1 limit of $m_z = 14.5$ used to define the initial complete sample in Paper I. Although the deeper CfA2 survey reveals no new cluster members, the complete sample as defined in Paper I can now be extended by 11 faint but known cluster members. The *B*, *R*, *I*, and *K'* photometry from Paper I is still nearly complete for this extended complete sample, but not all galaxies in the 14.5–15.5 mag range have H I synthesis data presented in Paper IV. Therefore, the initially defined complete sample of galaxies brighter than $m_z = 14.5$ will be considered here with less uncertainty about its completeness. The updated distance of 18.6 Mpc implies that all galaxies intrinsically brighter than $M_B = -16.8$ are considered in this paper.

This is roughly twice the intrinsic luminosity of the Small Magellanic Cloud.

Sticking to the CfA1 completeness limit, a volume-limited complete sample of 62 galaxies can be constructed from the sample of 79 cluster members identified in Paper I. However, not all of these galaxies are suitable for a TF study as a result of their low inclinations. Therefore, a lower inclination limit of 45°, based on optical axis ratios and an assumed intrinsic thickness of $q_0 = 0.2$, is imposed, reducing the sample size from 62 to 49 galaxies. These 49 galaxies will be referred to as the complete sample. Positional and redshift information on these systems can be

TABLE 1

COORDINATES FOR ALL 49 MEMBERS OF THE UMA CLUSTER BRIGHTER THAN $M_B = -16.8$ AND MORE INCLINED THAN 45°

Name (1)	R.A. (2)	Decl. (3)	l (deg) (4)	b (deg) (5)	SGL (deg) (6)	SGB (deg) (7)	V_{sys} (km s^{-1}) (8)
UGC 6399.....	11 20 35.9	51 10 09	152.08	60.96	62.02	−1.53	860
UGC 6446.....	11 23 52.9	54 01 21	147.56	59.14	59.72	0.22	727
NGC 3718.....	11 29 49.9	53 20 39	147.01	60.22	60.71	0.72	1074
NGC 3726.....	11 30 38.7	47 18 20	155.38	64.88	66.21	−1.79	919
NGC 3729.....	11 31 04.9	53 24 08	146.64	60.28	60.74	0.91	1142
NGC 3769.....	11 35 02.8	48 10 10	152.72	64.75	65.74	−0.75	796
1135+48	11 35 09.2	48 09 31	152.71	64.77	65.75	−0.74	798
UGC 6667.....	11 39 45.3	51 52 32	146.27	62.29	62.67	1.47	1051
NGC 3870.....	11 43 17.5	50 28 40	147.02	63.75	64.17	1.42	822
NGC 3877.....	11 43 29.3	47 46 21	150.72	65.96	66.68	0.38	955
UGC 6773.....	11 45 22.1	50 05 12	146.89	64.27	64.67	1.57	995
NGC 3893.....	11 46 00.2	48 59 20	148.15	65.23	65.73	1.24	1034
NGC 3896.....	11 46 18.6	48 57 10	148.10	65.29	65.78	1.27	913
NGC 3917.....	11 48 07.7	52 06 09	143.65	62.79	62.97	2.74	1046
UGC 6818.....	11 48 10.1	46 05 09	151.76	67.78	68.54	0.47	862
NGC 3949.....	11 51 05.5	48 08 14	147.63	66.40	66.83	1.70	865
NGC 3953.....	11 51 12.4	52 36 18	142.21	62.59	62.68	3.36	1137
UGC 6894.....	11 52 47.3	54 56 08	139.52	60.63	60.59	4.43	944
NGC 3972.....	11 53 09.0	55 35 56	138.85	60.06	59.98	4.72	951
UGC 6917.....	11 53 53.1	50 42 27	143.46	64.45	64.61	3.06	988
NGC 3985.....	11 54 06.4	48 36 48	145.94	66.27	66.56	2.34	1016
UGC 6923.....	11 54 14.4	53 26 19	140.51	62.06	62.07	4.09	1151
NGC 3992.....	11 55 00.9	53 39 11	140.09	61.92	61.91	4.27	1139
NGC 3990.....	11 55 00.3	55 44 13	138.25	60.04	59.95	5.01	696[a]
NGC 4013.....	11 55 56.8	44 13 31	151.86	70.09	70.77	1.06	880
NGC 4010.....	11 56 02.0	47 32 16	146.68	67.36	67.69	2.26	966
UGC 6969.....	11 56 12.9	53 42 11	139.70	61.96	61.92	4.46	1210
UGC 6973.....	11 56 17.8	43 00 03	153.97	71.10	71.94	0.68	743
UGC 6983.....	11 56 34.9	52 59 08	140.27	62.62	62.61	4.26	1170
NGC 4026.....	11 56 50.7	51 14 24	141.94	64.20	64.27	3.68	1023[a]
NGC 4051.....	12 00 36.4	44 48 36	148.88	70.08	70.51	2.04	753
NGC 4085.....	12 02 50.4	50 37 54	140.59	65.17	65.16	4.37	826
NGC 4088.....	12 03 02.0	50 49 03	140.33	65.01	65.00	4.46	838
UGC 7089.....	12 03 25.4	43 25 18	149.90	71.52	71.99	2.05	818
NGC 4100.....	12 03 36.4	49 51 41	141.11	65.92	65.93	4.23	1151
UGC 7094.....	12 03 38.5	43 14 05	150.14	71.70	72.19	2.02	827
NGC 4102.....	12 03 51.3	52 59 22	138.08	63.07	62.99	5.29	937
NGC 4111.....	12 04 31.0	43 20 40	149.53	71.69	72.13	2.20	815[a]
NGC 4117.....	12 05 14.2	43 24 17	149.07	71.72	72.13	2.35	998
UGC 7129.....	12 06 23.6	42 01 08	151.00	72.99	73.47	2.11	977[b]
NGC 4138.....	12 06 58.6	43 57 49	147.29	71.40	71.70	2.83	946
NGC 4143.....	12 07 04.6	42 48 44	149.18	72.40	72.79	2.47	985[c]
NGC 4157.....	12 08 34.2	50 45 47	138.47	65.41	65.33	5.27	857
NGC 4183.....	12 10 46.5	43 58 33	145.39	71.73	71.90	3.48	984
NGC 4218.....	12 13 17.4	48 24 36	138.88	67.88	67.81	5.27	804
NGC 4217.....	12 13 21.6	47 22 11	139.90	68.85	68.82	4.96	1097
NGC 4220.....	12 13 42.8	48 09 41	138.94	68.13	68.07	5.26	988
NGC 4346.....	12 21 01.2	47 16 15	136.57	69.39	69.30	6.17	783[a]
NGC 4389.....	12 23 08.8	45 57 41	136.73	70.74	70.65	6.16	786

NOTE.—Units of right ascension are hours, minutes, and seconds, and units of declination are degrees, arcminutes, and arcseconds.

[a] Redshift from RC3.

[b] Redshift from Falco et al. 1999.

[c] Redshift from di Nella et al. 1995.

found in Table 1. Column (1) gives the NGC or UGC number. Columns (2) and (3) provide the equatorial coordinates in B1950. Columns (4) and (5) provide the Galactic coordinates. Columns (6) and (7) contain the supergalactic longitude (SGL) and latitude (SGB). Column (8) gives the systemic velocity $V_{sys} = V_{hel} + 300 \sin l \cos b$, where V_{hel} is taken from Paper IV unless noted otherwise.

Note that the UMa Cluster is located in the supergalactic plane at about the same redshift as the core of the Virgo Cluster. Figure 1 shows the distribution on the sky and in redshift space of the complete sample. The cluster is diffuse and somewhat elongated along the supergalactic plane without any central condensation or large-scale morphological segregation. There seems to be a trend of systemic velocity with SGL suggesting some substructure or possible rotation of the galaxy ensemble.

2.1. *TF Scatter due to Depth Effects*

Since all galaxies are nearly at the same distance, there is little doubt about their relative luminosities, sizes, and masses. However, the UMa Cluster extends roughly $8° \times 15°$ on the sky, elongated along the supergalactic plane. Consequently, the depth of the sample may be considerable. The depth of the cluster is estimated by assuming that the distribution of all 79 identified cluster galaxies along the line of sight is similar to the distribution along SGL. From this assumption it follows that the estimated depth of the cluster contributes roughly $\sigma_{depth} = 0.17$ mag to the total observed scatter in the TF relation.

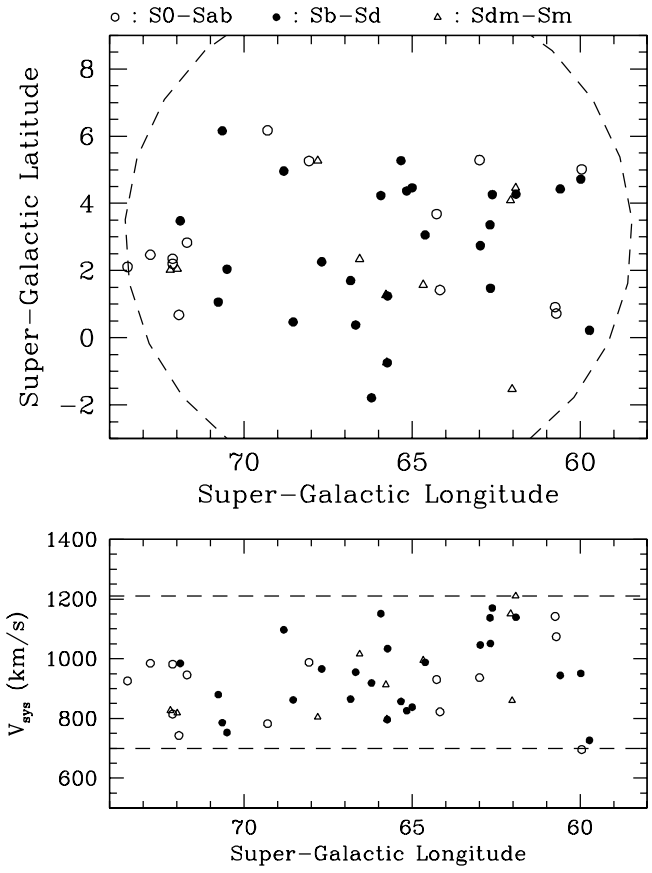

FIG. 1.—Distribution on the sky and in redshift of all 49 galaxies in the cluster brighter than $M_B = -16.8$ and more inclined than 45° (the complete sample). The dashed lines indicate the boundaries of the spatial and velocity window in which the galaxies were selected.

This estimate of the depth is a conservative lower limit since the UMa Cluster is located near the triple-value point of the projected velocity field induced by the gravitational potential of the Virgo Cluster. Consequently, significant velocity crowding occurs in the direction of the UMa Cluster, and the cluster's velocity range of $700 < V_{sys} < 1210$ km s^{-1} could cover as much as a factor of 2.1 in distance between the near and the far side of the volume (e.g., Fig. 2 in Davis & Peebles 1983). From this, a reasonable upper limit to the depth of the cluster follows by stretching the sample along this fully permitted line of sight, contributing a maximum of $\sigma_{depth} = 0.28$ mag to the total observed scatter in the TF relation for a slope of -10. However, in the remainder of this paper, $\sigma_{depth} = 0.17$ mag will be assumed. It should be noted that the effect of velocity crowding could lead to some contamination by galaxies, found in the cluster's limited velocity range, that are located significantly more nearby or farther away than the main body of the cluster.

3. AVAILABLE DATA

Table 2 compiles the available relevant photometric and kinematic data required to construct the various TF relations as well as some global parameters useful for searching for second parameters. Column (1) gives the NGC or UGC number. Columns (2)–(5) provide the total optical B_J, R_{KC}, I_{KC}, and near-infrared K' magnitudes corrected for Galactic and internal extinction as described in Paper IV. Total apparent magnitudes were taken from Paper I. Uncertainties in the total apparent magnitudes are estimated at 0.05 mag in the B, R, and I passbands and 0.08 mag in the K' passband. These estimates are based on comparisons of the derived luminosities of galaxies that were observed during different runs. Column (6) gives the adopted inclination and its estimated uncertainty as motivated in Paper IV. Column (7) contains the width of the global H I profile corrected for instrumental resolution, random motions, and inclination as described in Paper IV. There are four S0 galaxies (NGC 3990, NGC 4111, NGC 4143, NGC 4346) in which no H I could be detected. Column (8) contains information on the shape of the H I rotation curves. See § 4 for details. Column (9) provides the inclination-corrected maximum rotational velocities V_{max} measured from the H I rotation curves. For galaxies with a rising "R curve," V_{max} is the velocity of the last measured point. For galaxies with a flat "F curve," V_{max} is the rotational velocity averaged over the outer flat part. For galaxies with a declining "D curve," V_{max} represents the peak velocity. Column (10) gives the inclination-corrected amplitude of the flat part of the rotation curve. For galaxies with an R curve, V_{flat} could not be measured. For galaxies with an F curve, $V_{flat} = V_{max}$. For galaxies with a D curve, V_{flat} is the rotational velocity averaged over the outer flat part in which case $V_{flat} < V_{max}$. See § 4 for a detailed explanation. Column (11) gives the morphological type of the galaxy. Column (12) contains the inclination-corrected central disk surface brightness in the K' band, taken from Paper II. HSB galaxies are those galaxies with $\mu_0^i(K') < 18.5$, while LSB galaxies have $\mu_0^i(K') > 18.5$. Column (13) gives the exponential disk scale lengths in arcminutes, measured in the near-infrared. Column (14) provides the compactness parameter C_{82}, which is the ratio of the radii containing 80% and 20% of the total light, averaged over the B, R, and I bands. In some sense this is a measure of the bulge-disk ratio. Column (15) gives the inte-

TABLE 2

VARIOUS PROPERTIES OF THE COMPLETE SAMPLE

NAME (1)	$M_B^{b,i}$ (mag) (2)	$M_R^{b,i}$ (mag) (3)	$M_I^{b,i}$ (mag) (4)	$M_{K'}^{b,i}$ (mag) (5)	INCL. (deg) (6)	$W^i_{R,I}$ (km s^{-1}) (7)	SHAPE (8)	V_{max} (km s^{-1}) (9)	V_{flat} (km s^{-1}) (10)	TYPE (11)	$\mu^i_0(K')$ (mag arcsec^{-1}) (12)	$h_{K'}$ (arcmin) (13)	C_{82} (14)	$\int S dv$ (Jy km s^{-1}) (15)	$F_{60\ \mu m}$ (Jy) (16)	$F_{100\ \mu m}$ (Jy) (17)	$F_{1.4\ GHz}$ (mJy) (18)	SUBSAMPLES H I (19)	SI (20)	RC (21)	DE (22)	COMM. (23)
UGC 6399...	−17.56	−18.44	−18.77	−20.33	75±2	172±2	*R/F*	88±5	88±5	Sm	20.12	0.44	3.3	10.5±0.3	<0.17	<0.43	<2.5	×	×	*F*		1
UGC 6446...	−18.08	−18.72	−18.90	−19.88	51±3	174±8	*F, L*	82±4	82±4	Sd	19.84	0.33	4.1	40.6±0.5	<0.23	<0.52	<7.2	×	×	*F*	×	1
NGC 3718...	−20.90	−21.99	−22.54	−24.00	69±3	476±10	*F*	232±11	232±11	Sa	18.45	0.94	4.6	140.9±0.9	0.70±0.07	2.29±0.27	11.4±0.4	×	×			2
NGC 3726...	−20.76	−21.67	−22.07	−23.45	53±2	330±9	*F/(D)*	162±9	162±9	SBc	17.72	0.63	3.1	89.8±0.8	3.50±0.21	16.95±0.85	49.7±5.0	×	×	*F*		3
NGC 3729...	−19.34	−20.62	−21.22	−22.78	49±3	295±14	*F*	151±11	151±11	SBab	16.86	0.31	3.5	5.5±0.3	2.68±0.16	7.38±0.44	18.0±0.9	×	×	*F*		
NGC 3769...	−19.32	−20.35	−20.80	−22.35	70±2	257±8	*F/(D)*	122±8	122±8	SBb	17.62	0.33	3.6	62.3±0.6	2.63±0.13	6.78±0.41	12.1±2.9	×	×			4
1135+48	−16.67	−17.51	−17.88	−19.40	73±3	111±2	Confused	...	...	Sm	20.11	0.23	3.6	6.6±0.1	Confused	Confused	<1.6	×				4
UGC 6667...	−17.83	−18.87	−19.18	−20.65	89±1	167±2	*R/F, L*	86±3	86±3	Scd	20.44	0.54	3.3	11.0±0.4	<0.09	<0.76	<2.7	×	×	*F*	×	1
NGC 3870...	−17.83	−18.74	−19.26	−20.64	48±3	127±23	...	...	...	S0a	17.44	0.12	7.3	5.6±1.6	1.09±0.07	2.52±0.18	7.1±1.1	×				5, 6, 7
NGC 3877...	−20.60	−21.73	−22.29	−23.76	76±1	335±6	*F, L*	167±11	167±11	Sc	17.12	0.52	3.2	19.5±0.6	5.67±0.23	20.30±0.81	35.6±2.4	×	×	*F*	×	
UGC 6773...	−17.09	−17.87	−18.28	−20.14	58±3	113±5	*R, L*	45±5	...	Sm	19.48	0.28	3.3	5.6±0.4	<0.20	<0.62	<2.6	×	×	*R*		1
NGC 3893...	−20.55	−21.45	−21.86	−23.56	49±2	382±12	*F/(D)*	188±11	188±11	Sc	17.15	0.45	4.7	69.9±0.5	12.40±1.12	37.80±1.89	137.4±2.9	×	×			8
NGC 3896...	−17.69	−18.45	−18.92	−20.01	48±3	83±4	Confused	...	...	Sm	18.81	0.19	6.4	2.5±0.1	Confused	Confused	<3.1	×				8
NGC 3917...	−19.65	−20.63	−21.05	−22.40	79±2	275±3	*F*	135±3	135±3	Scd	18.66	0.57	3.0	24.9±0.6	0.61±0.05	3.16±0.22	<7.2	×	×	*F*	×	
UGC 6818...	−17.40	−18.10	−18.46	−19.71	75±3	151±3	*R/(F), L*	73±5	73±5	Sd	20.08	0.33	3.4	13.9±0.2	<0.15	<0.43	2.4±1.0	×	×			1, 9
NGC 3949...	−20.22	−20.96	−21.31	−22.98	55±2	320±8	*F, L*	164±7	164±7	Sbc	17.08	0.32	3.7	44.8±0.4	10.42±0.63	24.94±1.25	134.1±3.6	×	×	*F*	×	
NGC 3953...	−21.05	−22.20	−22.74	−24.41	62±1	446±5	*F*	223±5	223±5	SBbc	17.22	0.71	4.4	39.3±0.8	3.68±0.18	28.49±7.69	50.9±2.5	×	×	*F*		
UGC 6894...	−16.51	−17.39	−17.59	−19.01	83±3	124±1	*R*	63±5	...	Scd	20.35	0.28	3.1	5.8±0.2	<0.16	<0.44	<2.7	×	×	*R*	×	1
NGC 3972...	−19.08	−20.05	−20.48	−22.08	77±1	264±2	*R, L*	134±5	...	Sbc	17.90	0.36	3.0	16.6±0.4	1.01±0.06	3.66±0.22	<5.8	×	×	*R*	×	
UGC 6917...	−18.63	−19.49	−19.84	−21.10	56±2	224±7	*R/F*	104±4	104±4	SBd	19.83	0.54	3.4	26.2±0.3	0.26±0.04	1.02±0.18	<4.4	×	×	*F*	×	
NGC 3985...	−18.39	−19.30	−19.69	−21.19	51±3	180±9	*R*	93±7	...	Sm	17.56	0.21	2.9	15.7±0.6	1.42±0.09	3.42±0.24	9.7±1.4	×	×	*R*		10
NGC 6923...	−17.84	−18.67	−19.20	−20.36	65±2	160±4	*R, L*	81±5	...	Sdm	18.80	0.24	5.0	10.7±0.6	0.37±0.04	0.90±0.19	<2.6	×	×	*R*		
NGC 3992...	−21.18	−22.28	−22.80	−24.21	56±2	547±13	*F/D*	272±6	242±5	SBbc	17.45	0.77	4.0	74.6±1.5	1.12±0.07	10.35±0.52	30.2±7.6	×	×	*D*		
NGC 3990...	−17.89	−19.31	−20.02	−21.82	63±3	...	...	...	...	S0	16.79	0.15	8.5	...	<0.17	<0.32	<1.4					1, 6, 11
NGC 4013...	−20.08	−21.40	−22.07	−23.83	90±1	377±1	*F/D*	195±3	177±6	Sb	16.44	0.38	3.7	41.5±0.2	5.70±0.34	20.13±1.81	36.3±0.8	×	×	*D*	×	3
NGC 4010...	−19.30	−20.17	−20.55	−22.31	89±1	254±1	*(R)/F, L*	128±9	128±9	SBd	19.41	0.64	2.9	38.2±0.3	1.68±0.15	6.76±0.34	16.9±1.6	×	×	*F*	×	3
UGC 6969...	−16.56	−17.28	−17.48	−18.80	76±2	117±7	*R*	79±5	...	Sm	20.34	0.25	3.0	6.1±0.5	<0.10	<0.48	<3.8	×	×	*R*		1
UGC 6973...	−19.21	−20.67	−21.28	−23.23	71±3	363±7	*F/D*	173±10	173±10	Sab	15.72	0.18	5.3	22.9±0.2	...	...	127.5±2.1	×	×			12
UGC 6983...	−18.58	−19.31	−19.61	−20.87	49±1	222±4	*F*	107±7	107±7	SBcd	19.87	0.49	3.8	38.5±0.6	0.29±0.06	1.34±0.20	<5.4	×	×	*F*	×	
NGC 4026...	−19.74	−21.16	−21.82	−23.71	84±3	385±11	...	...	...	S0	17.13	0.43	7.3	...	<0.12	<0.52	<1.4	×				1, 6, 11
NGC 4051...	−20.71	−21.72	−22.18	−23.54	49±3	309±14	*R/F, L*	159±13	159±13	SBbc	17.18	0.50	4.0	35.6±0.8	7.14±0.93	23.92±1.20	26.5±2.6	×	×			13
NGC 4085...	−19.12	−20.11	−20.57	−22.27	82±2	247±7	*R/F, L*	134±6	134±6	Sc	17.36	0.29	3.2	14.6±0.9	5.49±0.27	14.61±0.73	44.1±1.3	×	×	*F*	×	
NGC 4088...	−20.95	−21.94	−22.45	−24.00	69±2	362±5	*F/(D), L*	173±14	173±14	Sbc	17.25	0.62	3.0	102.9±1.1	19.88±0.99	54.47±2.72	222.3±1.9	×	×	*F*		
UGC 7089...	−18.11	−18.96	−19.26	−20.30	80±3	138±2	*R, L*	79±7	...	Sdm	20.53	0.57	3.5	17.0±0.6	...	...	<3.4	×	×	*R*		
NGC 4100...	−20.51	−21.49	−21.97	−23.48	73±2	386±5	*F/D*	195±7	164±13	Sbc	17.11	0.47	2.9	41.6±0.7	8.10±0.49	21.72±0.87	54.3±1.7	×	×	*D*	×	
UGC 7094...	−16.67	−17.69	−18.16	−19.78	70±3	76±3	*R, L*	35±6	...	Sdm	19.68	0.27	4.5	2.9±0.2	...	...	<2.6	×	×	*R*		
NGC 4102...	−19.86	−21.20	−21.73	−23.57	56±2	393±10	*F*	178±11	178±11	SBab	16.78	0.33	7.6	8.0±0.2	46.90±1.88	69.74±2.79	276.0±1.5	×	×	*F*		14
NGC 4111...	−20.01	−21.44	−22.13	−23.76	90±3	...	...	...	...	S0	17.25	0.40	7.8	...	...	...	9.7±0.6					6, 11
NGC 4117...	−17.36	−18.92	−19.57	−21.38	68±3	251±10	...	...	...	S0	18.01	0.20	6.1	6.9±1.1	...	...	3.7±1.2	×				15
UGC 7129...	−17.36	−18.65	−19.23	...	48±3	96±8	...	...	...	Sa	...	...	4.4	...	...	...	<1.4	×				6, 16
NGC 4138...	−19.50	−20.93	−21.50	−23.22	53±3	374±16	*F/D*	195±7	147±12	Sa	16.48	0.26	5.3	19.2±0.7	...	...	16.7±4.6	×	×	*D*		
NGC 4143...	−19.35	−20.83	−21.54	−23.50	60±3	...	...	...	...	S0	15.89	0.23	8.0	...	...	...	10.8±1.0					6, 17
NGC 4157...	−20.72	−21.83	−22.33	−24.04	82±3	398±4	*F/D*	201±7	185±10	Sb	16.77	0.48	3.9	107.4±1.6	12.01±0.72	45.43±2.27	179.6±2.3	×	×	*D*	×	
NGC 4183...	−19.46	−20.16	−20.46	−21.74	82±2	228±2	*F/D, L*	115±6	109±4	Scd	19.47	0.59	3.2	48.9±0.7	...	...	<5.8	×	×	*D*	×	
NGC 4218...	−17.88	−18.68	−19.06	−20.55	53±3	150±9	*R*	73±7	...	Sm	17.06	0.12	3.2	7.8±0.2	1.09±0.08	2.29±0.23	6.3±0.8	×	×	*R*		
NGC 4217...	−20.33	−21.54	−22.16	−23.90	86±2	381±5	*F/D*	191±6	178±5	Sb	17.17	0.54	3.3	33.8±0.7	8.88±0.62	35.35±2.47	115.6±2.2	×	×	*D*	×	
NGC 4220...	−20.03	−21.29	−21.91	−23.13	78±3	399±5	...	...	...	Sa	16.55	0.29	4.2	4.4±0.3	1.57±0.13	5.53±0.50	<4.9	×				15
NGC 4346...	−19.27	−20.70	−21.42	−23.15	77±3	...	...	...	...	S0	17.13	0.33	8.2	...	...	...	<1.4					6, 11
NGC 4389...	−19.05	−20.21	−20.63	−22.27	50±4	212±12	*R*	110±8	...	SBbc	17.07	0.27	3.6	7.6±0.2	...	...	23.3±1.2	×	×			18

NOTE.—Cols. (19)–(22) indicate to which subsample a galaxy belongs. A letter refers to the rotation curve shape as explained in § 4. Comments: (1) 5 σ upper limits to the *IRAS* flux given the rms noise in the median co-added local *IRAS* scan. (2) Anomalous; extreme warp, conspicuous dust lane. (3) Strongly warped. (4) Interacting pair NGC 3769/1135+48. (5) H I data from Fisher & Tully 1981. (6) 1.4 GHz flux or upper limit from the NVSS. (7) Mrk 186. (8) Interacting pair NGC 3893/NGC 3896. (9) Interacting with faint dwarf? (10) Anomalous; extreme warp, optically disturbed. (11) Optical redshift from RC3. (12) Interacting with UGC 6962. (13) Strongly lopsided, Seyfert. (14) H I in absorption against nucleus, LINER. (15) Too little H I to retrieve V_{max} or V_{flat}. (16) Optical redshift from Falco et al. 1999. (17) Optical redshift from di Nella et al. 1995. (18) Bar dominated. Table 2 is also available in machine-readable form in the electronic edition of the *Astrophysical Journal*.

grated H I flux density as measured from the global H I profile. Columns (16) and (17) contain the *IRAS* 60 and 100 μm fluxes taken from the *IRAS* Faint Source Catalog. Upper limits were obtained using SCANPI, available at IPAC, and represent 5 times the noise level in the median co-added local *IRAS* scans. A total of 11 galaxies are unfortunately located in the infamous *IRAS* gap. Column (18) gives the 21 cm radio continuum flux density taken from Paper IV. Flux densities and upper limits for galaxies not listed in Paper IV were taken from the NVSS (Condon et al. 1998). Columns (19)–(22) show to which subsample each galaxy is assigned. The various subsamples are explained in § 5. Column (23) contains references to comments listed in a note to the table.

4. H I ROTATION CURVE SHAPES

The available radio synthesis data presented in Paper IV provide H I rotation curves that, for now, can be classified in three categories as illustrated in Figure 2.

First, there are rotation curves that keep on rising continuously until the last measured point (*left panel*). In these cases, the observed maximum rotational velocity is determined by the extent of the H I disk and provides a lower limit to the actual maximum rotational velocity induced by the gravitational potential. This type of rotation curve is often observed in dwarf galaxies and in spirals with an H I disk that is confined to the inner regions. The global H I profiles of these galaxies are in general Gaussian or boxy and lack a clear double-peaked signature. These rising rotation curves will be referred to as "*R* curves" hereafter.

Second, there are the "classical" rotation curves that show a modest rise in the inner regions and then gently bend over to reach a more or less extended flat part in the outer regions of the galaxy (*middle panel*). This behavior is typical for Sb- to Sd-type spirals. In a standard rotation curve decomposition, the amplitude of the flat part corresponds to the maximum rotational velocity induced by the dark matter halo (e.g., van Albada & Sancisi 1986). The global profiles of these galaxies usually show a clear double-peaked profile, and the amplitude of the flat part can in general be well retrieved from the width of the global H I profile. The selection criteria outlined by Bernstein et al. (1994) are aimed at selecting galaxies with such a classical rotation curve like NGC 3917, based on their global properties. These kinds of "classical" flat rotation curves will be referred to as "*F* curves."

Third, there are the partly declining rotation curves that show a steep rise in the inner regions and reach a peak rotational velocity well within the stellar disk, often induced by a massive bulge component (*right panel*). After this maximum they show a modest decline within the observed stellar disk, typically beyond two to three disk scale lengths. In most cases this decline halts and the rotation curve extends farther out with a more or less constant rotational velocity. This behavior of the rotation curves is often seen in massive early-type spirals and in galaxies with a compact distribution of their luminous matter (e.g., Casertano & van Gorkom 1991). In these systems, a distinction can be made between the maximum rotational velocity $V_{\rm max}$ of the peak in the rotation curve and the amplitude of its more or less extended flat part $V_{\rm flat}$. These rotation curves with $V_{\rm max} > V_{\rm flat}$ will be referred to as "*D* curves" hereafter.

Of course, there are many intermediate cases and cases in which one side of the galaxy does show a flat part while the other side is still rising. There are also rotation curves that are kinematically lopsided in the sense that one side is rising more steeply than the other side.

Figure 2 demonstrates that the rotational velocity of a spiral galaxy is not very well defined. The horizontal arrows in Figure 2 indicate the rotational velocities as derived from the corrected global H I profiles. In the case of NGC 3917, the amplitude of the flat part can be retrieved well from the global profile. In the case of NGC 4389, the amplitude of the flat part cannot be measured from the width of the global profile simply because it is not sampled by the H I disk that is confined to the inner regions of the galaxy. In the case of NGC 3992, the width of the global profile yields the maximum rotational velocity $V_{\rm max}$ and not the amplitude $V_{\rm flat}$ of the outer flat part. This situation arises because the bulk of the H I gas is located near the maximum rotational velocity. In general, the rotational velocities derived from the global profiles of galaxies with declining rotation curves depend on where the bulk of the H I gas is located along the rotation curve.

Note that $V_{\rm max}$ and $V_{\rm flat}$ were not just measured from position-velocity diagrams as depicted in Figure 2. They

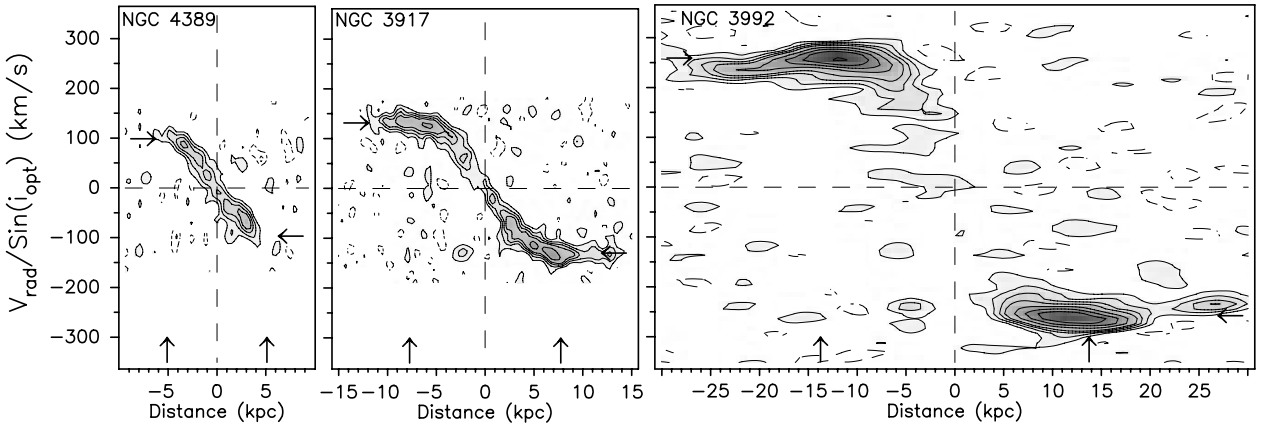

FIG. 2.—Prototype examples of the three categories of rotation curves. *Left:* Galaxy with a rotation curve that rises continuously until the last measured point. The measured maximum rotational velocity $V_{\rm max}$ is set by the extent of the H I disk (*R* curve). *Middle:* "Classical" rotation curve; a gentle rise in the central regions with a smooth transition into the extended flat part (*F* curve). *Right:* Rotation curve that reaches a maximum in the optical regions after which it declines somewhat to an extended flat part in the outer disk. In this case, the maximum rotation velocity exceeds the amplitude of the flat part (*D* curve). The vertical arrows indicate $\pm R_{25}$, and the horizontal arrows indicate the rotational velocities as inferred from the global profiles.

were measured from the rotation curves determined by fitting tilted rings to the two-dimensional velocity fields as explained in Paper IV.

The examples in Figure 2 illustrate how the width of a global H I profile is determined not only by the intrinsic maximum rotational velocity of a galaxy but also by the actual shape of the rotation curve and the distribution of the H I gas. Even when the line width is measured with great accuracy, it does not guarantee a precise measurement of V_{max} or V_{flat}. Note, however, that early-type spirals are often excluded in studies of the TF relation as a distance tool since inclusion of these galaxies is known to increase the scatter in the relation (e.g., Rubin et al. 1985; Pierce & Tully 1988). From an H I perspective, an increased scatter for early-type systems might be related to their relative small H I content (e.g., Fig. 5 in Paper IV), which could give a patchy sampling of the rotation curve along the kinematic major axis.

5. SUBSAMPLES

The availability, quality, and characteristics of the H I velocity fields and rotation curves warrant the construction of various subsamples drawn from the complete sample. Furthermore, using the TF relation as an empirical distance estimator requires a different approach to galaxy selection procedures compared to its use for constraining galaxy formation scenarios. In the first case, galaxies are, often subjectively, selected on the basis of the regularity of their morphology and other global properties with the sole purpose to minimize the scatter in the observed relation. In the second case, searching for the underlying physical basis of the TF relation, it is important to recognize to what extent the H I kinematics conveys information about the gravitational potentials of galaxies with a wide variety of global properties. With these considerations in mind, the following subsamples were constructed.

5.1. *The* H I *Sample*

There are 45 galaxies in the complete sample that have a measured H I global profile. These 45 galaxies will be referred to as the H I sample. Most of these profiles are presented in Paper IV. There is one single-dish profile (NGC 3870), while three global H I profiles (NGC 4026, NGC 4117, UGC 7129) were obtained with a new deep VLA H I survey of parts of the UMa Cluster. This new survey aims at measuring the slope of the H I mass function at the faint end, and its results will be presented in a forthcoming paper in this series. The H I sample will be used to construct TF relations for the largest possible sample, invoking no selection criteria while using global H I profile widths only, thereby ignoring any detailed kinematic information. One of the goals of this paper is to understand the scatter in this H I sample using information from the H I rotation curves.

5.2. *The DE Sample*

When using the TF relation as an empirical distance estimator one cannot afford to obtain H I rotation curves of each galaxy to investigate its kinematic state. Therefore, galaxies are usually selected on the basis of their global optical morphology and the shape of their global (single-dish) H I profiles. To determine how the current UMa sample would "perform" as a distance estimator, galaxies were selected from the H I sample according to the same selection criteria as outlined by Bernstein et al. (1994). In their study of spirals around the Coma Cluster they only selected noninteracting galaxies of type Sb–Sd, with steep H I profile edges, with smooth outer isophotes, and without a prominent bar. These criteria are somewhat subjective, but they are based on global morphological characteristics that do not require detailed kinematic information on individual systems. Table 3 summarizes which galaxies from the H I sample are excluded by these criteria. There are 16 galaxies that survive the various selection criteria, and those 16 will be referred to as the DE sample. Because evaluation of these criteria is somewhat subjective, the reader is encouraged to examine the actual data presented in Papers I and IV.

5.3. *The SI Sample*

There are 38 galaxies in the H I sample for which useful synthesis imaging data are available. These 38 galaxies will be referred to as the SI sample, and their H I data are presented in detail in Paper IV. From these synthesis imaging data, the kinematic state of the galaxies could be determined and for most galaxies the shape of their H I rotation curves could be measured. The galaxies 1135+48, NGC 3870, NGC 3896, NGC 4026, NGC 4117, UGC 7129, and NGC 4220 did not make it from the H I sample into the SI sample because of confusion and signal-to-noise issues.

5.4. *The RC Sample*

Not all galaxies in the SI sample are kinematically well enough behaved to allow the measurement of a reliable rotation curve that assumes that the H I clouds are on stable orbits around the galaxy center. Although judging the kinematic state of a galaxy is somewhat subjective, seven galaxies in the SI sample were identified as being too disturbed for determining a reliable rotation curve.

From the H I velocity fields and column density maps it is clear that several galaxies in the SI sample are involved in interactions (NGC 3769, NGC 3893, UGC 6818, UGC

TABLE 3

GALAXIES EXCLUDED FROM THE H I SAMPLE BASED ON THE SELECTION CRITERIA BY BERNSTEIN ET AL. (1994)

Criteria	Excludes
Noninteracting	NGC 3769, NGC 3893, UGC 6973, UGC 6818
Sb–Sd morphology	NGC 3718, NGC 3729, NGC 3870, UGC 6973, NGC 4102, UGC 7129, NGC 4138, NGC 4220 (earlier types), UGC 6399, UGC 6773, NGC 3985, UGC 6923, UGC 6969, UGC 7089, UGC 7094, NGC 4218 (later types)
No prominent bar	NGC 3726, NGC 3729, NGC 3769, NGC 3953, NGC 3992, NGC 4010, NGC 4051, NGC 4102, NGC 4389
Smooth outer isophotes.....	NGC 3718, NGC 3893, UGC 6973, UGC 6818, NGC 3985, NGC 4051, NGC 4088
Steep H I profile edges	NGC 3769, NGC 3985, NGC 4218

NOTE.—Several galaxies are excluded for more than one reason.

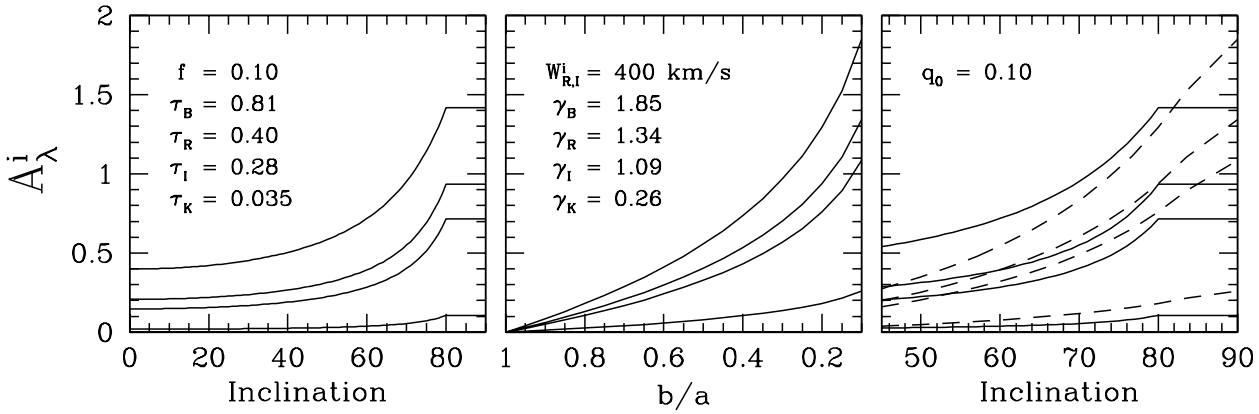

FIG. 3.—Comparison of the two most commonly used correction methods for internal extinction. *Left:* TF85 model. *Middle:* γ log (a/b) scheme. *Right:* Two models overlayed. See § 6 for details.

6973) evidenced by tidal H I tails and disturbed velocity fields. NGC 3718 is extremely warped, while the Seyfert galaxy NGC 4051 is very lopsided. It seems very likely that the assumption of stable closed orbits is violated in these systems. One galaxy (NGC 4389) only shows H I emission along its prominent bar in which case the "rotation curve" merely reflects streaming motions and the bar pattern speed. In these cases the H I kinematics is unlikely to be a useful tracer of the gravitational potential of the galaxies, and the rotation curves of these galaxies cannot be determined with much confidence. There are 31 galaxies in the SI sample for which a useful H I rotation curve could be measured, and these 31 galaxies are referred to as the RC sample.

Within the RC sample, there are nine galaxies with an *R* curve that make up the RC/*R* sample, 15 galaxies with an *F* curve that make up the RC/*F* sample, and seven galaxies with a *D* curve that make up the RC/*D* sample. Consequently, there are 22 galaxies in the RC sample for which $V_{\rm flat}$ could be measured with some confidence. These 22 galaxies make up the combined RC/*FD* sample (RC/*F* + RC/*D*) and include galaxies with Sa–Sm morphologies, barred galaxies, and galaxies with mild kinematically lopsided rotation curves in their inner regions.

6. INTERNAL EXTINCTION CORRECTIONS

The correction for internal extinction is most uncertain and significantly affects the slope, zero point, and scatter of the TF relation in the optical passbands. Therefore, it deserves some special attention. It is worth pointing out the differences between the two most widely used correction methods to appreciate their influences on the statistical properties of the TF relations. One of the two main correction schemes was proposed by TF85, where

$$A^i_\lambda = -2.5 \times \log\left[f(1 + e^{-\tau_\lambda \sec i}) + (1 - 2f)\left(\frac{1 - e^{-\tau_\lambda \sec i}}{\tau_\lambda \sec i}\right)\right],$$

with f the fraction of stars above and below a slab of dust in which the fraction (1–2f) of the stars is homogeneously mixed with the dust. The opacity of the face-on dust layer is given by τ_λ. For inclinations above 80°, $A^{i>80}_\lambda = A^{i=80}_\lambda$ motivated by the idea that the stars behind the slab of dust become visible once the disk is sufficiently inclined. This "TF85 model" also corrects for internal extinction in face-on galaxies. This is a more or less physically motivated model, and the values of f and τ_B were initially estimated by TF85 at $f = 0.25$ and $\tau_B = 0.55$. The Galactic reddening law was used to adopt τ_λ in the other passbands. This correction scheme, with updated values for f and τ_λ, was used in Paper I to obtain extinction-corrected magnitudes.

The other main correction scheme (e.g., Giovanelli et al. 1994) is more empirical in nature and takes the form

$$A^{i\to 0}_\lambda = -\gamma_\lambda \log\left(\frac{a}{b}\right),$$

where γ_λ is wavelength dependent and (a/b) is the observed optical axis ratio. Note that this model only corrects toward a face-on situation; it does not correct for extinction in face-on galaxies for which $(a/b) = 1$. The values of γ_λ are determined by minimizing the observed scatter in the TF relations, an exercise performed by many investigators in the past. For instance, Tully et al. (1998) used the present UMa sample combined with a sample of galaxies in Perseus-Pisces to find that γ_λ also depends on the absolute galaxy luminosity; brighter galaxies contain relatively more obscuring dust than fainter galaxies. The absolute magnitude can be expressed in terms of the distance-independent line width through the TF relations themselves via an iterative scheme. Eventually, γ_λ can be expressed as

$$\gamma_\lambda = \alpha_\lambda + \beta_\lambda(\log W^i_{R,I} - 2.5),$$

where the values of α_λ and β_λ are given in § 2 of Paper IV and $\gamma_\lambda = 0$ in the case $W^i_{R,I} < 85$ km s^{-1}. Since γ_λ depends on the line width, a major consequence is that it affects the slope of the TF relation, which becomes steeper when using the latter correction scheme compared to the TF85 model. Table 1 of Paper IV contains the applied internal extinction corrections for each individual galaxy in each of the four passbands based on the $-\gamma_\lambda$ log (a/b) scheme. Corrections can be as high as 1.40, 1.02, 0.82, and 0.20 mag in the *B*, *R*, *I*, and *K*′ passbands, respectively. Using data from all four passbands, a "redder than Galactic" reddening law was found and explained by Tully et al. (1998).

It will be obvious that for highly inclined systems, the uncertainties in the internal extinctions at *B*, *R*, and *I* become quite substantial even without considering galaxy-to-galaxy variations in (f, τ_λ) or γ_λ. For instance, no distinc-

tion is made between dusty HSB galaxies and the relatively dust-free LSB galaxies of similar $W^i_{R,I}$.

The difference between the two corrections schemes is illustrated in Figure 3. The four lines in each panel correspond to the four different passbands considered here. The uppermost line represents the larger B-band correction. In the left panel A^i_λ is plotted against inclination for the TF85 model. Note the nonzero correction for face-on galaxies and the constant correction for highly inclined systems. The middle panel shows $A^{i\to 0}_\lambda$ as a function of (b/a) for a corrected global H I line width of $W^i_{R,I} = 400$ km s^{-1}. Note the zero correction for face-on systems. The amplitudes of the curves in the middle panel increase with increasing line width. For a line width of 85 km s^{-1} or less, all the correction curves become zero. The right panel compares the two models over a range of inclinations relevant for the current study. An intrinsic thickness of $q_0 = 0.1$ was adopted to convert (b/a) into an inclination angle. Considering the B-band correction for edge-on systems, differences between the two models can be as large as 0.5 mag for massive systems and -1.4 mag for dwarf galaxies with $W^i_{R,I} < 85$ km s^{-1}. These considerations alone strongly support the use of K' luminosities, thus minimizing the uncertainties that come with the internal extinction corrections.

7. TF RELATIONS

In this section the TF relations will be discussed in the various bandpasses using the different kinematic measures $W^i_{R,I}$, $V_{\rm max}$, and $V_{\rm flat}$. First the applied methods of fitting and calculating the total observed scatter will be described. Then the TF relations for the H I and DE samples using the global H I profile widths will be discussed. Next, the shapes of the rotation curves will be used to explain the larger scatter and shallower slopes found in the H I sample.

7.1. *Fitting Method*

For each passband and kinematic measure a straight line of the form

$$M = a + b \log W$$

was fitted to the data points, where M is the corrected absolute magnitude and $\log W$ is either $\log W^i_{R,I}$, $\log (2V_{\rm max})$, or $\log (2V_{\rm flat})$. Inverse least-squares fits were made by minimizing

$$\chi^2(a', b') = \sum_{i=1}^{N} \frac{[\log W_i - (a' + b' M_i)]^2}{\sigma^2_{\log W_i} + b'^2 \sigma^2_{M_i}}$$

and thus taking errors in both directions into account. The zero point a and slope b of the TF relation can then be recovered according to $a = -a'/b'$ and $b = 1/b'$. The error σ_M in the absolute magnitude not only accounts for measurement errors of the actual luminosity but also accommodates contributions to the scatter from uncertainties due to the depth of the sample and a possible intrinsic scatter:

$$\sigma^2_M = \sigma^2_{M^{b,i}_{\rm obs}} + \sigma^2_{\rm depth} + \sigma^2_{\rm intr} .$$

As argued in § 2, it can be expected that $\sigma_{\rm depth} \approx 0.17$ mag. However, in practice $\sigma_{\rm depth}$ and $\sigma_{\rm intr}$ cannot be separated. Therefore, in calculating $\chi^2_{\rm red}$, it was decided to keep $\sigma_{\rm depth} = 0$ and $\sigma_{\rm intr} = 0$ initially. In § 9 it will be explored how much of this additional scatter can be allowed for by $\chi^2_{\rm red}$.

After the inverse least-squares fits are made, a weighted total observed rms scatter $\sigma_{\rm obs}$ can be calculated according to

$$\sigma^2_{\rm obs} = \frac{\sum_{i=1}^{N} w_i [M_i - (a + b \log W_i)]^2}{\sum_{i=1}^{N} w_i} ,$$

with the weights w_i calculated according to

$$w_i = \frac{1}{\sigma^2_{M_i} + b^2 \sigma^2_{\log W_i}} .$$

This formalism assumes that the errors σ_M and $\sigma_{\log W_i}$ are independent and of a Gaussian nature. Unfortunately, this is not quite the case.

When calculating σ_{M_i} and $\sigma_{\log W_i}$, the following measurement errors can be considered. First, there are the photometric uncertainties σ_{m_T} in the total apparent magnitude, which are estimated at 0.05 mag in the optical passbands and 0.08 mag in the near-infrared band. These errors are estimated by comparing total apparent magnitudes of galaxies observed during several of the 14 observing runs (see Paper I). However, uncertainties vary from galaxy to galaxy, and the values quoted above just reflect the rms scatter of the differences. Second, there are the formal measurement errors $\sigma_{W_{20}}$ on the observed H I line widths W_{20}. Because the signal-to-noise ratio of the global H I profiles varies significantly from galaxy to galaxy, the formal measurement errors cover a wide range and, indeed, can be very small for high signal-to-noise profiles with steep edges. The values of $\sigma_{W_{20}}$ do not reflect differences in line widths caused by different measurement techniques (see Paper IV). Third, the uncertainties on $V_{\rm max}$ and $V_{\rm flat}$ as listed in Table 2 are not classical Gaussian 1 σ errors but rather reflect a fiducial range of values allowed by the H I position-velocity diagrams. Fourth, the inclinations and their uncertainties are estimated using various different observations like optical axis ratios, ellipticities of H I disks, tilted ring fits to velocity fields, and morphologies of dust lanes. Consequently, the uncertainties in the inclination angles σ_i are not Gaussian in nature (e.g., $89° \pm 1°$).

Apart from the non-Gaussian observational errors, there are also uncertainties associated with the models used to correct the raw data for Galactic and internal extinction, instrumental velocity resolution, and turbulent motions of the H I gas. The parameters used in the models to correct for internal extinction $(\alpha_\lambda, \beta_\lambda)$ and turbulent motions $(W_{c,20}, W_{t,20})$ have only a statistical meaning (see Paper IV). Consequently, estimates of their uncertainties are dictated by the concept of the model and lose their meaning in any Gaussian error propagation exercise. One should also keep in mind that the values of $(\alpha_\lambda, \beta_\lambda)$ were determined in an iterative way by minimizing the observed scatter in the TF relation in the first place. Finally, note that the values of $M^{b,i}_T$ and $\log W^i_{R,I}$ and their errors are not entirely independent because $M^{b,i}_T$ depends to some extent on $W^i_{R,I}$ through the correction for internal extinction; a larger value of $W^i_{R,I}$ implies a larger internal extinction correction, depending on (b/a), and thus a brighter absolute magnitude.

All these considerations make a rigorous statistical treatment of the observed scatter in the TF relation practically impossible, and one might argue against a $1/\sigma^2$ weighting altogether. Therefore, in practice, inverse least-squares fits with equal weights (i.e., all points have similar errors) were made by assuming that all galaxies have equal relative

uncertainties of 5% in $W^i_{R,I}$, V_{max}, or V_{flat} and equal photometric uncertainties of 0.05 mag in $M^{b,i}_T(B, R, I)$ and 0.08 mag in $M^{b,i}_T(K')$. These estimated average uncertainties allow one to calculate a fiducial value of χ^2_{red} in order to evaluate the necessity of any intrinsic scatter to explain the total observed scatter. Note that the adopted photometric uncertainties in the optical absolute magnitudes are probably underestimates given the applied corrections for internal extinction.

The total observed scatter was calculated according to

$$\sigma^2_{obs} = \frac{\sum_{i=1}^{N} w_i[M^{b,i}_T(\mathrm{obs})_i - (a + b \log W_i)]^2}{\sum_{i=1}^{N} w_i},$$

where w_i was calculated as above and "a" and "b" are the fitted zero point and slope of the TF relation. In practice, w_i is identical for all galaxies.

Since the rms scatter may be strongly affected by outliers, it often does not represent the scatter of the bulk of the data points. Therefore, it is useful to calculate the more robust bi-weight scatter σ^{bi} (Beers, Flynn, & Gebhardt 1990) as well. Values of σ^{bi} were determined after a normal least-squares fit was made. For a pure Gaussian distribution of residuals one would find $\sigma^{rms} = \sigma^{bi}$.

Finally, it should be noted that a tighter TF relation does not necessarily imply a better distance tool. The tightness of the relation is expressed by χ^2_{red}, which is calculated by considering errors in both directions. The usefulness of the TF relation as a distance tool, however, depends on the scatter in the direction of the luminosity axis, which is related to the steepness of the slope. Consequently, a tighter correlation with a steeper slope may still display a larger scatter along the luminosity axis.

The results of the inverse least-squares fits in the various passbands for the various subsamples are listed in Table 4.

7.2. *TF Relations Using Global Profiles*

Figure 4 shows the TF relations in each of the four passbands, constructed with the corrected widths of the global profiles $W^i_{R,I}$. First, the full H I sample will be considered. In the upper panels, all 45 galaxies in the H I sample are plotted, regardless of their morphologies, H I profile shapes, and kinematic state. In the upper K' panel, UGC 7129 is missing because it lacks a K' magnitude measurement. Table 4 lists the results of the inverse least-squares fits. The scatters are similar ($\sim$0.6 mag) in the four passbands although the slope is steepening systematically from -6.8 to -8.0 going from the blue to the near-infrared. The total observed scatters in the H I sample are far larger than can be explained by the estimated measurement uncertainties as suggested by $\chi^2_{red} \gg 1$, while there are no significant indications for curvature or other deviations from a linear relation. Note that the bi-weight scatter is slightly smaller than the rms scatter, indicating that there are non-Gaussian outliers in the distribution of residuals. One such outlier in the optical passbands is NGC 4117, a rather red dwarf lenticular galaxy (see Paper I). It seems to be underluminous in the blue passband, but it systematically shifts toward the relation going farther to the (near-infra)red. The scatter in the H I sample demonstrates that the TF relations are of limited use as distance estimators if no further selection criteria are imposed.

The lower panels in Figure 4 show the TF relations for the 16 regular galaxies in the restricted DE sample that were selected on the basis of their global morphological properties. Obviously, selecting galaxies on the basis of

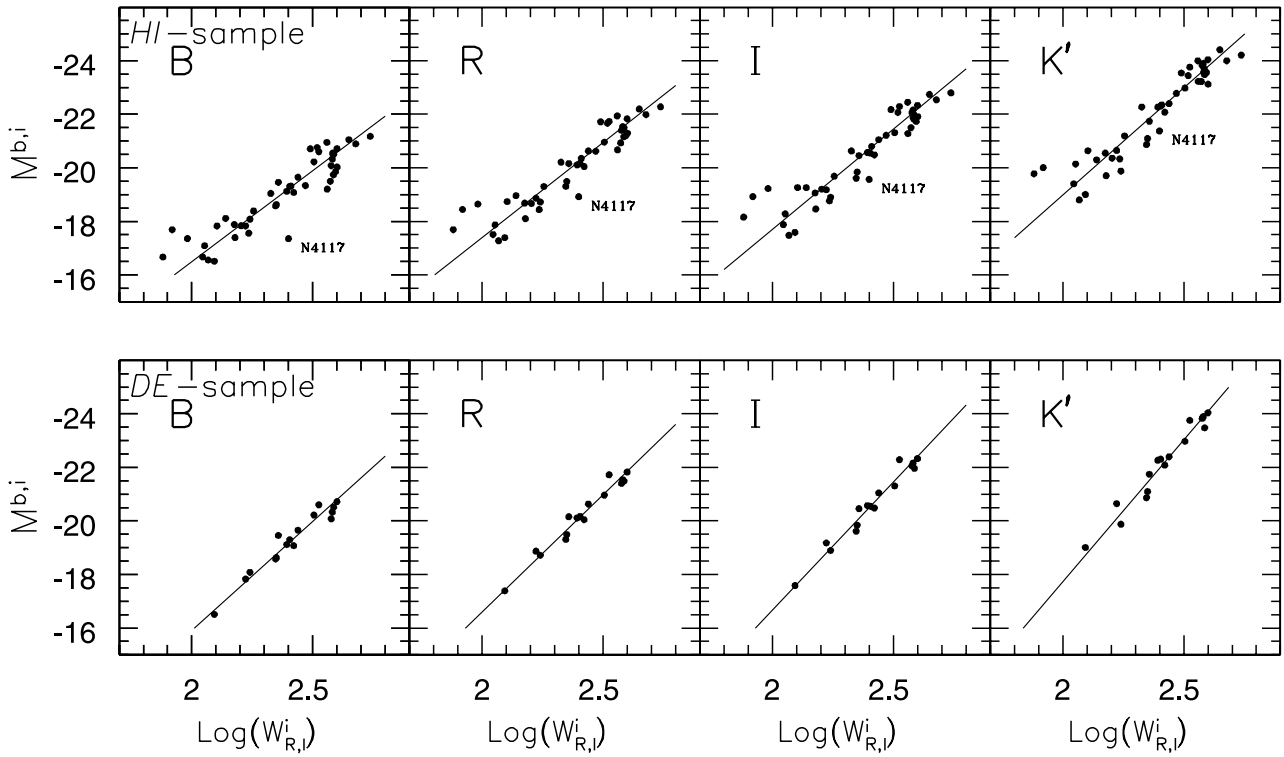

FIG. 4.—TF relations using the corrected widths $W^i_{R,I}$ of the global H I profiles. *Upper panels:* TF relations for all 45 galaxies in the H I sample. *Lower panels:* TF relations for the 16 galaxies in the strictly selected DE sample. Solid lines show the results of the inverse least-squares fits to these particular subsamples. Note that the DE sample displays steeper and tighter correlations with less scatter, illustrating the merit of imposing selection criteria when using the TF relation as a distance estimator.

TABLE 4

RESULTS FROM INVERSE LEAST-SQUARES LINEAR FITS TO THE VARIOUS SAMPLES

		ZERO POINT			SLOPE			SCATTER						χ^2_{red}		
								rms			Bi-Weight					
BAND	N	$W^i_{R,I}$ (mag)	$2V_{max}$ (mag)	$2V_{flat}$ (mag)	$W^i_{R,I}$	$2V_{max}$	$2V_{flat}$	$W^i_{R,I}$ (mag)	$2V_m$ (mag)	$2V_f$ (mag)	$W^i_{R,I}$ (mag)	$2V_m$ (mag)	$2V_f$ (mag)	$W^i_{R,I}$	$2V_m$	$2V_f$
H I Sample																
B.....	45	-2.91 ± 0.33			-6.8 ± 0.1			0.61			0.56			15.8		
R	45	-3.15 ± 0.33			-7.1 ± 0.1			0.56			0.52			12.3		
I	45	-2.73 ± 0.34			-7.5 ± 0.1			0.61			0.53			13.1		
K'.....	44	-2.98 ± 0.33			-8.0 ± 0.1			0.59			0.55			9.8		
DE Sample																
B.....	16	0.40 ± 0.80			-8.2 ± 0.3			0.28			0.29			2.5		
R	16	0.90 ± 0.82			-8.8 ± 0.4			0.24			0.25			1.6		
I	16	2.49 ± 0.83			-9.6 ± 0.4			0.26			0.26			1.6		
K'.....	16	3.45 ± 0.95			-10.6 ± 0.4			0.32			0.34			1.9		
SI Sample																
B.....	38	-2.09 ± 0.37			-7.1 ± 0.1			0.48			0.48			8.9		
R	38	-1.96 ± 0.38			-7.6 ± 0.1			0.45			0.43			7.0		
I	38	-1.33 ± 0.39			-8.0 ± 0.2			0.49			0.47			7.4		
K'.....	38	-1.77 ± 0.45			-8.5 ± 0.2			0.55			0.49			7.7		
RC/*FDR* Sample																
B.....	31	-2.37 ± 0.41	-2.14 ± 0.41		-7.0 ± 0.1	-7.1 ± 0.1		0.45	0.55		0.45	0.54		8.0	12.0	
R	31	-2.19 ± 0.42	-1.95 ± 0.43		-7.5 ± 0.2	-7.6 ± 0.2		0.43	0.55		0.40	0.46		6.5	10.5	
I	31	-1.49 ± 0.43	-1.19 ± 0.44		-8.0 ± 0.2	-8.1 ± 0.2		0.48	0.61		0.45	0.43		7.3	11.6	
K'.....	31	-1.92 ± 0.48	-1.62 ± 0.49		-8.4 ± 0.2	-8.5 ± 0.2		0.56	0.71		0.48	0.44		8.1	12.8	
RC/*FD* Sample																
B.....	22	0.37 ± 0.74	0.36 ± 0.74	1.66 ± 0.79	-8.1 ± 0.3	-8.1 ± 0.3	-8.7 ± 0.3	0.44	0.47	0.39	0.46	0.48	0.41	6.1	6.9	4.2
R	22	0.50 ± 0.75	0.41 ± 0.75	2.01 ± 0.81	-8.6 ± 0.3	-8.5 ± 0.3	-9.2 ± 0.4	0.35	0.37	0.31	0.37	0.38	0.33	3.4	3.9	2.3
I	22	1.74 ± 0.76	1.59 ± 0.76	3.37 ± 0.83	-9.2 ± 0.3	-9.2 ± 0.3	-10.0 ± 0.4	0.36	0.37	0.31	0.37	0.37	0.33	3.1	3.4	2.1
K'.....	22	2.25 ± 0.84	1.94 ± 0.83	3.96 ± 0.93	-10.1 ± 0.4	-10.0 ± 0.4	-10.8 ± 0.4	0.40	0.38	0.32	0.40	0.33	0.32	3.1	2.8	1.8
RC/*F* Sample																
B.....	15	2.55 ± 0.94		2.85 ± 0.96	-9.0 ± 0.4		-9.2 ± 0.4	0.38		0.39	0.33		0.42	3.8		3.8
R	15	2.81 ± 0.96		3.09 ± 0.98	-9.6 ± 0.4		-9.7 ± 0.5	0.32		0.31	0.32		0.35	2.4		2.3
I	15	4.09 ± 0.99		4.33 ± 1.00	-10.2 ± 0.5		-10.4 ± 0.5	0.33		0.31	0.33		0.35	2.3		2.0
K'.....	15	4.68 ± 1.09		4.74 ± 1.09	-11.1 ± 0.5		-11.2 ± 0.5	0.35		0.26	0.40		0.28	2.0		1.1
RC/*FD* Sample, Excluding NGC 3992																
B.....	21	1.35 ± 0.82	1.34 ± 0.82	2.46 ± 0.87	-8.5 ± 0.4	-8.5 ± 0.4	-9.0 ± 0.4	0.45	0.48	0.40	0.45	0.49	0.41	5.7	6.5	4.0
R	21	1.45 ± 0.82	1.34 ± 0.82	2.81 ± 0.88	-9.0 ± 0.4	-8.9 ± 0.4	-9.6 ± 0.4	0.33	0.36	0.30	0.35	0.38	0.32	2.9	3.4	2.1
I	21	2.79 ± 0.83	2.60 ± 0.83	4.27 ± 0.89	-9.7 ± 0.4	-9.6 ± 0.4	-10.4 ± 0.4	0.33	0.35	0.30	0.35	0.35	0.32	2.5	2.7	1.7
K'.....	21	3.58 ± 0.93	3.19 ± 0.92	5.12 ± 1.00	-10.6 ± 0.4	-10.5 ± 0.4	-11.3 ± 0.5	0.34	0.31	0.26	0.35	0.31	0.27	2.0	1.7	1.1

NOTE.—Results from inverse least-squares linear fits to the various samples, taking errors of 5% in $W^i_{R,I}$, V_{max}, and V_{flat} into account as well as uncertainties of 0.05 mag in the optical passbands and 0.08 mag in the K' passband. It is assumed that $\sigma^2_{depth} + \sigma^2_{intr} = 0$.

their regular appearance greatly reduces the scatter to 0.24–0.32 mag, although χ^2_{red} indicates that the scatters are still somewhat larger than can be expected from the measurement uncertainties, even when taking the depth effect into account. The rms and bi-weight scatters are similar for the DE sample, indicating that outliers are effectively eliminated. The systematic steepening of the slope toward the near-infrared is maintained in the DE sample, but the slopes have become steeper for each passband, ranging from -8.2 to -10.6 going from the blue to the near-infrared. These steeper slopes are a result of the fact that the selection criteria for the DE sample eliminate galaxies in certain areas of the TF diagrams. As a consequence of the steeper slopes, the zero points have changed significantly given the current formulation $M = a + b \log W$ for the TF relation (see Table 4). The DE sample also illustrates that a smaller scatter does not imply a tighter relation. Comparing the B- and K'-band relations, one finds $\sigma_{rms} = 0.28$ and $\chi^2_{red} = 2.5$ for the B band while $\sigma_{rms} = 0.32$ and $\chi^2_{red} = 1.9$ for the K' band.

At this point, one can argue that the R-band TF relation provides the best distance estimator since it displays the smallest scatter. However, it is not entirely obvious whether the H I or the DE sample should be used to provide upper limits on the intrinsic scatter as a constraint on galaxy formation scenarios, although the tightness of the K' relation and the uncertainties related to the extinction corrections in the optical seem to make the near-infrared relation more relevant.

One of the main purposes of this paper is to investigate whether the larger scatter and shallower slopes in the H I sample can be understood given the available detailed kinematic information in the form of H I velocity fields and rotation curves. One might also want to investigate whether the scatter in the DE sample can be reduced even further by using information from the H I rotation curves instead of the width of the global H I profiles. These issues will be addressed in the next subsection.

7.3. *TF Relations and the Shapes of Rotation Curves*

Figure 5 shows the TF relations in all four passbands, constructed for the RC sample of 31 galaxies that have measured rotation curves. The TF relations in the upper panels were constructed using the corrected widths of the global profiles $W^i_{R,I}$. The relations in the middle panels were constructed using V_{max} from the rotation curves. The lower panels show the relations using the amplitude V_{flat} of the flat part of the rotation curve. The various symbols refer to the shapes of the rotation curves: open triangles for galaxies with rising R curves (nine points), filled circles for galaxies with flat F curves (15 points), and open circles for galaxies with declining D curves (seven points). Crosses indicate galaxies in the SI sample that are excluded from the RC sample because they are involved in strong interactions or have severe kinematic distortions that lead to an unreliable determination of their rotation curves (seven points). The open triangles could not be included in the lower panels simply because V_{flat} cannot be measured for R curves.

The results of the various inverse linear least-squares fits with equal weights are collected in Table 4. As a reminder, weights are based on a 0.05 mag error in the optical magnitudes, a 0.08 mag error in the near-infrared magnitudes, and a 5% uncertainty in either $W^i_{R,I}$, $2V_{max}$, or $2V_{flat}$. The values of χ^2_{red} quoted in Table 4 are based on $\sigma^2_{depth} + \sigma^2_{intr} = 0$ in order to illustrate to what extent the estimated observational errors can explain the total observed scatter. Separate fits were made to the various RC subsamples, thereby ignoring the crosses. To allow a meaningful comparison of the statistical properties of the correlation for the three kinematic measures at a certain passband, one should consider the same subsamples in all three of the rows. Therefore, fits in the upper and middle panels were also made considering only those galaxies that appear in the lower panels for a certain subsample.

The solid lines in Figure 5 indicate the least-squares fits to the 15 filled symbols of the RC/F sample only. The dashed lines show the fits to the entire RC sample (31 galaxies in the upper and middle panels and 22 galaxies in the lower panels). From Figure 5 and Table 4 the following can be noted.

First of all, the 15 galaxies in the RC/F sample with a "classical" rotation curve (F curves with $V_{max} = V_{flat}$; *filled circles*) define a steeper and tighter relation (*solid lines*) compared to the entire RC sample (*dashed lines*). This happens to be the case in all passbands using any of the three kinematic measures. However, when using V_{flat} (*lower panels*), the differences between the solid and dashed lines are insignificant.

Second, galaxies with a rotation curve that is still rising at the last measured point (R curves with no V_{flat}; *open triangles*) lie systematically on the low-velocity side of the relations defined by the galaxies with F curves (*solid lines*). These galaxies with R curves are mainly found among the fainter systems in the sample. If the H I disks of those galaxies would have been more extended, they most likely would have probed higher velocities farther out into the halo, and consequently those galaxies would have shifted to the right, i.e., toward the relation.

Third, galaxies with a partly declining rotation curve (D curves with $V_{max} > V_{flat}$; *open circles*) in the upper and middle panels tend to lie systematically on the high-velocity side compared to galaxies with $V_{max} = V_{flat}$ of the same luminosity. If the lower amplitude V_{flat} of the flat part is used instead of the higher V_{max} values, these galaxies shift to the left, i.e., toward the relation, and line up with galaxies that have a "classical" F curve as illustrated in the lower panels. Galaxies with declining rotation curves are mainly found among the brightest systems in the sample and are in general of earlier morphological type.

Fourth, the tightest relation with the smallest scatter is found for the 15 galaxies in the RC/F sample using K' magnitudes and $2V_{flat}$ as the kinematic measure ($\sigma_{rms} = 0.26$ and $\chi^2_{red} = 1.1$).

The $M^{b,i}_{K'}$–log ($2V_{flat}$) relation for the 22 galaxies in the RC/FD sample gives a less tight correlation with a larger scatter. However, this can be entirely attributed to one single galaxy, NGC 3992, represented by the most upper right open circle in each panel of Figure 5. Excluding NGC 3992 from the RC/FD sample reduces the rms scatter significantly from 0.32 to 0.26 mag and χ^2_{red} from 1.8 to 1.1; the same statistical results are found for the smaller sample of 15 galaxies in the RC/F sample. The reason why NGC 3992 is not detected as an outlier through the bi-weight scatter is the fact that it is at the extreme end of the correlation and therefore it pulls the slope of the least-squares fit toward it, thereby significantly reducing its residual. Making an inverse fit to the $M^{b,i}_{K'}$–log ($2V_{flat}$) correlation of the RC/

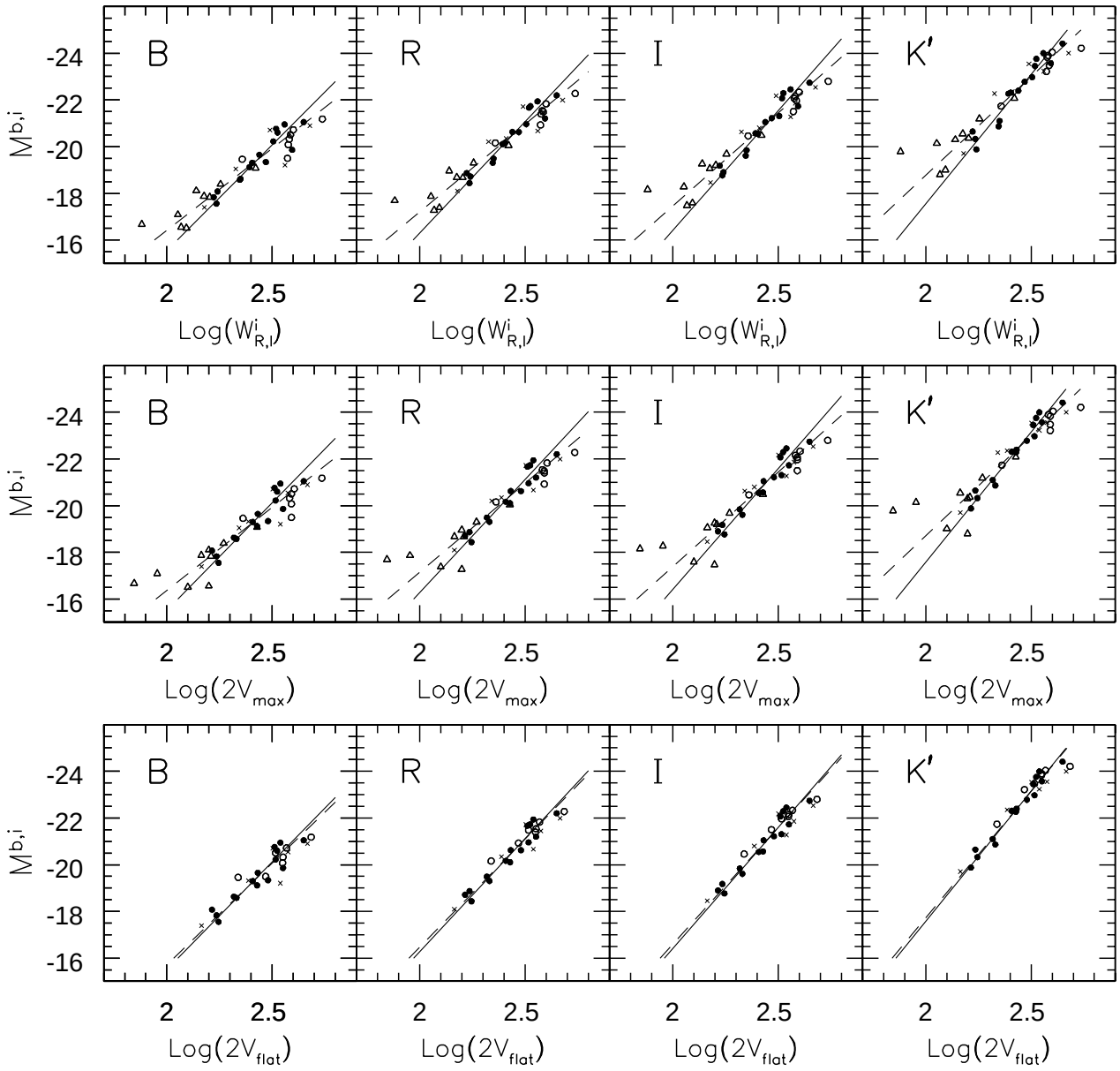

FIG. 5.—TF relations for all 31 galaxies in the RC sample with measured rotation curves (*circles and triangles*). The crosses indicate the additional seven galaxies in the SI sample for which a reliable rotation curve could not be measured. Those seven galaxies were ignored when making the inverse least-squares fits. The TF relations are constructed for each of the four available passbands using three different kinematic measures: the corrected width $W^i_{R,I}$ of the global H I profile (*upper panels*), the maximum rotational velocity V_{max} measured from the H I rotation curve (*middle panels*), and the amplitude of the flat part V_{flat} of the H I rotation curve (*lower panels*). The open triangles indicate galaxies with *R* curves, the open circles indicate galaxies with *D* curves, and the filled symbols indicate galaxies with *F* curves. Solid lines show the fits to the 15 filled circles only. The dashed lines show fits using all galaxies from the RC sample in each panel.

$FD^{\rm NGC\,3992}$ sample and subsequently calculating the scatters including NGC 3992 yields $\sigma^{\rm rms} = 0.35$ mag and $\sigma^{\rm bi} = 0.31$ mag, a small but significant difference. Removing the most deviating galaxy in the RC/$FD^{\rm NGC\,3992}$ sample (NGC 3953, $\Delta M = -0.51$ mag) does not significantly reduce the scatter any further.

It is conceivable that NGC 3992 is a background galaxy given its high recession velocity of $V_{\rm sys} = 1139$ km s^{-1}. Its companions UGC 6923 and UGC 6969 also have high systemic velocities of 1151 and 1210 km s^{-1}, respectively, straddling the high-velocity edge of the cluster's 700–1210 km s^{-1} velocity window. Furthermore, note that UGC 6969, the lower open triangle, also lies significantly below the relation. Assuming that the NGC 3992 group is 50% farther away than the UMa Cluster as a whole, which is not inconceivable given the velocity crowding in the UMa region, would put NGC 3992 and UGC 6969 back on the TF relation while UGC 6923 moves slightly farther away from the relation, making it stand out more as a galaxy with an *R* curve (*open triangle*).

Finally, removing NGC 3992 from the RC/*FD* sample and considering the remaining 21 galaxies in the RC/$FD^{\rm NGC\,3992}$ sample, the correlation becomes robust, progressively tighter, and steeper and displays less scatter going from the blue to the near-infrared (see Table 4). Furthermore, for the RC/$FD^{\rm NGC\,3992}$ sample, the correlation also tightens when using $V_{\rm flat}$ instead of $V_{\rm max}$ from the rotation curve.

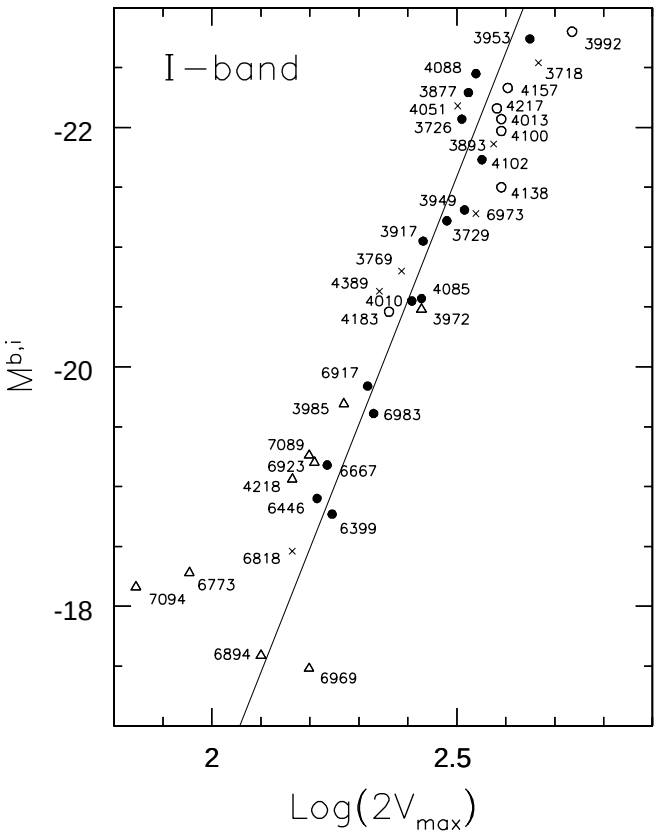

FIG. 6.—Enlargement of the *I*-band panel in the middle panels of Fig. 5. Here the symbols are labeled with a galaxy's NGC or UGC number to allow checking with the photometric and H I synthesis data of Papers I and IV. NGC numbers run from 3718 through 4389, UGC numbers run from 6399 through 7094.

For the skeptical reader, Figure 6 provides a blowup of the *I*-band panel in the middle row of Figure 5. Each symbol is labeled with the NGC or UGC numbers used in the various tables throughout this paper. This allows for relating each individual data point to its observational data presented in Papers I and IV.

8. SEARCHING FOR A SECOND PARAMETER

Even though $\sigma_{\rm depth} = 0$, the least-squares fit results for the 21 galaxies in the RC/$FD^{\rm NGC\,3992}$ sample show $\chi^2_{\rm red} = 1.1$ in the case of the K' band, and no significant correlation of the residuals with other parameters can be expected. However, in the *B* band $\chi^2_{\rm red} = 4.0$, which leaves room for a possible second parameter to explain the excess of scatter. It should be remarked that taking $\sigma_{\rm depth} = 0.17$ mag into account, one finds $\chi^2_{\rm red} = 2.3$ and 0.7 for the *B*-band and K'-band relations, respectively, indicating a possible slight overestimation of the depth of the cluster or of the observational errors in the $M^{b,i}_{K'}$–log $(2V_{\rm flat})$ relation. The values of $\chi^2_{\rm red}$ quoted in the remainder of this section are based on $\sigma^2_{\rm depth} + \sigma^2_{\rm intr} = 0$ unless explicitly mentioned.

Figure 7 shows the residuals in the $M^{b,i}_{B,K'}$–log $(2V_{\rm flat})$ TF relations, as displayed in the lower panels of Figure 5, plotted against various global properties of the spirals. Only the *B*-band and K'-band residuals are considered as extreme cases. As usual, filled symbols indicate galaxies with *F* curves, and open symbols indicate galaxies with *D* curves. The crosses, indicating kinematically ill-behaved systems in Figure 5, are omitted since they were not included in the fits. The galaxy NGC 3992 is also excluded from all the fits and is indicated by an open symbol with a cross through it. Error bars are based on the estimated observational uncertainties and the slopes fitted to the 21 galaxies in the RC/$FD^{\rm NGC\,3992}$ sample. Note that there are only 17 galaxies with a measured far-infrared flux.

The dashed lines in Figure 7 are direct least-squares fits to the residuals, taking only the vertical error bars into account. For each panel, the number of points included in the fits as well as the resulting values of the slopes and $\chi^2_{\rm red}$ are listed in Table 5. The galaxy UGC 6399 is excluded from the fit in panel (3a) of Figure 7 because it clearly seems to break the trend set by earlier type systems while no other late-type galaxies are available to confirm any turnover.

Figure 1 hinted at a possible correlation between $V_{\rm sys}$ and SGL, and therefore the TF residuals are plotted versus systemic velocity and SGL in panels (1a), (1b), (2a), and (2b) of Figure 7. No significant correlations are found with respect to the positions of the galaxies in the cluster; the fitted slopes are not significantly different from zero, and the values of $\chi^2_{\rm red}$ are not significantly reduced. Nevertheless, the dashed line in panel (2b) has a slope consistent with the observation that galaxies at lower SGL have higher $V_{\rm sys}$ values (see Fig. 1) and thus might be farther away in case they are subjected to a Hubble flow. Consequently, they would be underluminous (negative residuals) under the assumption that all galaxies are at the same distance. However, $\chi^2_{\rm red}$ is reduced from 1.1 to 0.8, indicating that the noise is being fitted, while the slope deviates only 2.3 σ from zero. When invoking $\sigma_{\rm depth} = 0.17$, $\chi^2_{\rm red}$ reduces further to 0.5.

TABLE 5

VALUES OF $\chi^2_{\rm red}$ FROM LEAST-SQUARES FITS TO THE RESIDUALS, EXCLUDING NGC 3992 AND ASSUMING $\sigma_{\rm depth} = 0$

	B BAND			*K'* BAND		
PARAMETER	*N*	Slope	$\chi^2_{\rm red}$	*N*	Slope	$\chi^2_{\rm red}$
$V_{\rm sys}$	21	-0.00063 ± 0.00037	3.9	21	-0.00039 ± 0.00047	1.0
SGL	21	0.014 ± 0.013	4.0	21	0.038 ± 0.017	0.8
Type	20	0.15 ± 0.03	2.4	21	0.003 ± 0.029	1.1
cos *i*	21	-0.08 ± 0.19	4.0	21	-0.55 ± 0.24	0.8
$M_{\rm H\,I}/L_{K'}$	21	0.47 ± 0.08	2.4	21	0.03 ± 0.10	1.1
$L_{\rm FIR}/L_{K'}$	16	-0.32 ± 0.17	3.2	16	0.00 ± 0.22	0.9
$B-I$	21	-0.80 ± 0.13	2.2	21	-0.09 ± 0.17	1.0
$\mu^{b,i}_{0,K'}$	21	0.13 ± 0.03	3.3	21	0.016 ± 0.041	1.1

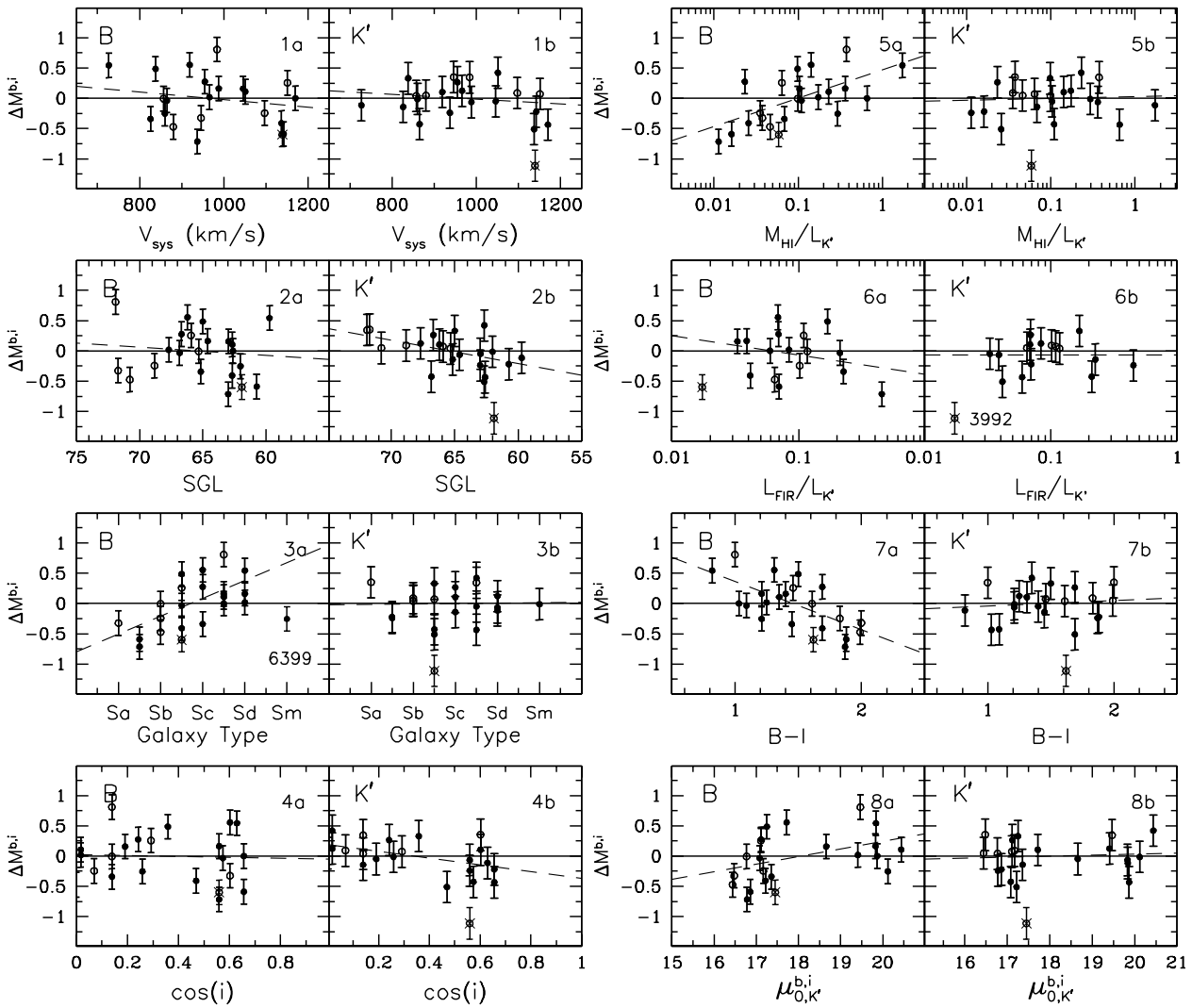

FIG. 7.—Residuals of the $M^{b,i}_{B,K'}$–log ($2V_{\rm flat}$) TF relations as a function of various global properties of the spiral galaxies: (1) systemic velocity, (2) SGL, (3) morphological type, (4) inclination angle, (5) relative H I content, (6) relative dust content, (7) global $B-I$ color, and (8) face-on central K' surface brightness of the fitted exponential disk. Only the 21 galaxies in the RC/$FD^{\rm NGC\,3992}$ sample are considered for the fits. The excluded galaxy NGC 3992 is indicated by the crossed out open circle. UGC 6399 was excluded from the fit in panel (3a). *Filled circles:* Galaxies with $V_{\rm max} = V_{\rm flat}$. *Open circles:* Galaxies with $V_{\rm max} > V_{\rm flat}$.

When inspecting Figure 7 and Table 5, it turns out that no significant second parameter can be found for the K' residuals. However, for the B-band residuals, several significant correlations with a second parameter are evident in panels (3a), (5a), (7a), and (8a). In those cases, the fitted slopes deviate from zero by 5.0, 5.9, 6.2, and 4.3 σ while $\chi^2_{\rm red}$ reduces from 4.0 to 2.4, 2.4, 2.2, and 3.3, respectively. However, most striking is the fact that these four significant correlations are consistent with each other in the sense that they reflect general trends along the Hubble sequence. Positive residuals are found for late-type spirals that in general are gas-rich and bluer with a lower surface brightness. Effectively, early-type spirals are too faint in their blue light or rotate too fast compared to late-type spirals. Because these correlations are absent when using K' magnitudes, the B-band correlations can be interpreted as the result of different stellar populations between early- and late-type spirals of the same luminosity and not as the results of differences in the rotational velocities $V_{\rm flat}$, induced by their dark matter halos. If early-type spirals would reside in more massive halos compared to their equiluminous late-type counterparts, a similar correlation with morphological type would have been observed for the K' residuals. In light of the uncertain internal extinction corrections, it is somewhat reassuring that no significant correlations are found between the B-band and K'-band residuals with inclination.

Correlations of the residuals in the TF relations with effective surface brightness and compactness of the radial light distribution were also found by Willick (1999), using R-band magnitudes and Hα long-slit rotation curves. He found that galaxies with a high effective surface brightness or a highly compact light distribution are too faint for their rotational velocity or rotate too fast for their luminosity; they lie systematically below the TF relation. Interestingly, this is consistent with results from Rubin et al. (1985), who found that early-type spirals lie systematically below the TF relation defined by later types (see also § 12). Courteau & Rix (1999) analyzed the residuals from a mean relation between parameterized velocities at 2.2 disk scale lengths and I- and r-band luminosities. They presented "tentative evidence" that the residuals correlate with disk scale lengths and that there is a "slight tendency" for them to

TABLE 6

95% CONFIDENCE INTERVALS FOR $(\sigma^2_{\rm depth} + \sigma^2_{\rm intr})^{1/2}$ AND FOR $\sigma_{\rm intr}$ IN THE CASE $\sigma_{\rm depth} = 0.17$

		$(\sigma^2_{\rm depth} + \sigma^2_{\rm intr})^{1/2}$			$\sigma_{\rm intr}$ ($\sigma_{\rm depth} = 0.17$)		
N	BAND	$W^i_{R,I}$ (mag)	$2V_{\rm max}$ (mag)	$2V_{\rm flat}$ (mag)	$W^i_{R,I}$ (mag)	$2V_{\rm max}$ (mag)	$2V_{\rm flat}$ (mag)
				H I Sample			
45.....	B	0.48–0.57–0.70			0.45–0.54–0.68		
	R	0.44–0.53–0.65			0.41–0.50–0.63		
	I	0.47–0.57–0.70			0.44–0.54–0.68		
	K'	0.46–0.56–0.69			0.43–0.53–0.67		
				DE Sample			
16.....	B	0.14–0.24–0.39			0.00–0.17–0.35		
	R	0.04–0.18–0.32			0.00–0.06–0.27		
	I	0.00–0.18–0.34			0.00–0.06–0.29		
	K'	0.11–0.26–0.44			0.00–0.20–0.41		
				SI Sample			
38.....	B	0.36–0.45–0.56			0.32–0.42–0.53		
	R	0.34–0.42–0.53			0.29–0.38–0.50		
	I	0.37–0.46–0.57			0.33–0.43–0.54		
	K'	0.42–0.52–0.65			0.38–0.49–0.63		
				RC/*FDR* Sample			
31.....	B	0.33–0.42–0.55	0.42–0.52–0.67		0.28–0.38–0.52	0.38–0.49–0.65	
	R	0.32–0.40–0.53	0.42–0.52–0.67		0.27–0.36–0.50	0.35–0.49–0.65	
	I	0.35–0.45–0.59	0.46–0.55–0.75		0.32–0.42–0.56	0.43–0.55–0.73	
	K'	0.42–0.53–0.69	0.54–0.68–0.87		0.38–0.50–0.67	0.51–0.66–0.85	
				RC/*FD* Sample			
22.....	B	0.30–0.41–0.56	0.33–0.43–0.60	0.25–0.35–0.49	0.25–0.37–0.53	0.28–0.39–0.58	0.18–0.31–0.46
	R	0.21–0.31–0.44	0.24–0.33–0.47	0.15–0.25–0.38	0.12–0.26–0.41	0.14–0.28–0.44	0.00–0.18–0.34
	I	0.21–0.31–0.45	0.22–0.33–0.47	0.14–0.25–0.38	0.12–0.26–0.42	0.17–0.28–0.44	0.00–0.18–0.34
	K'	0.24–0.35–0.51	0.21–0.32–0.47	0.11–0.24–0.38	0.17–0.31–0.48	0.12–0.27–0.44	0.00–0.17–0.34
				RC/*F* Sample			
15.....	B	0.23–0.36–0.55		0.23–0.36–0.56	0.15–0.32–0.52		0.15–0.32–0.53
	R	0.15–0.27–0.45		0.14–0.27–0.44	0.00–0.21–0.42		0.00–0.21–0.41
	I	0.15–0.28–0.47		0.11–0.25–0.43	0.00–0.22–0.44		0.00–0.18–0.39
	K'	0.13–0.28–0.49		0.00–0.14–0.33	0.00–0.22–0.46		0.00–0.00–0.28
				RC/*FD* Sample, Excluding NGC 3992			
21.....	B	0.30–0.41–0.57	0.33–0.44–0.61	0.25–0.35–0.50	0.25–0.37–0.54	0.28–0.41–0.59	0.18–0.31–0.47
	R	0.19–0.29–0.42	0.22–0.32–0.46	0.13–0.23–0.37	0.08–0.23–0.38	0.14–0.27–0.43	0.00–0.15–0.33
	I	0.17–0.27–0.41	0.19–0.29–0.44	0.08–0.21–0.35	0.00–0.21–0.37	0.08–0.23–0.41	0.00–0.12–0.31
	K'	0.14–0.26–0.41	0.09–0.22–0.37	0.00–0.10–0.27	0.00–0.20–0.37	0.00–0.14–0.33	0.00–0.00–0.21

NOTE.—The numbers for each entry refer to the minimum, the most likely, and the maximum intrinsic scatter.

correlate with color in the sense that redder disks with shorter scale lengths rotate faster than bluer and more extended disks of the same I- or r-band luminosity. The correlations found in these studies are consistent and in qualitative agreement with the current UMa results. However, as a result of the different data characteristics and analysis techniques, a more quantitative comparison is unfeasible.

9. INTRINSIC SCATTER

While reading the previous sections, it may have become clear that the scatter in the TF relation can be dramatically decreased by applying proper selection criteria and especially when detailed knowledge about the kinematics of individual spirals is available. However, the intrinsic scatter in the TF relation is an elusive concept, and its meaning depends on the context in which it is discussed. It has been shown that the statistical properties of the TF relation are closely related to the passband in which the luminosities are derived and to the selection criteria by which means the galaxy sample is constructed. Therefore, extreme care should be taken if one tries to relate the intrinsic scatter to a certain degree of noncircular motions induced by nonspherical halos when the intrinsic scatter is derived from a sample that is critically selected and optimized to serve as a distance tool (e.g., Franx & de Zeeuw 1992). On the other hand, it would be unfair to relate the intrinsic scatter to the degree of accuracy with which distances can be measured if the intrinsic scatter is derived from a complete volume-limited sample without any further selection criteria

applied. For instance, the critically selected DE sample yields a much tighter correlation than the volume-limited H I sample.

Given the estimated observational errors, the 95% confidence intervals for both $(\sigma^2_{\rm depth} + \sigma^2_{\rm intr})^{1/2}$ and the intrinsic scatter $\sigma_{\rm intr}$ were calculated assuming $\sigma_{\rm depth} = 0.17$ as motivated in § 2.1. These intervals indicate the minimum and maximum values of the (intrinsic) scatters that can be accommodated within the total observed scatter. The results for the various passbands, samples, and kinematic measures are collected in Table 6. The minimum scatter, the most likely scatter, and the maximum scatter are given for each entry. Note that, in general, the confidence intervals become broader with smaller numbers of galaxies in a sample and that, in principle, $\sigma_{\rm depth}$ and $\sigma_{\rm intr}$ cannot be separated.

9.1. *TF as a Distance Tool: The $M^{b,i}_{B,R,I,K'}$–log $W^i_{R,I}$ Relations*

When applying the TF relation as an empirical distance tool on large samples of galaxies, to measure large-scale cosmic velocity fields, for instance, it is impractical to obtain detailed kinematic information in the form of H I rotation curves for tens of thousands of galaxies. The WHISP project (Westerbork observations of neutral hydrogen in irregular and spiral galaxies) aims at gathering H I synthesis data of about 3000 H I–rich nearby systems. However, for all practical purposes, single-dish global H I profiles are used. Consequently, the $M^{b,i}_{B,R,I,K'}$–log $W^i_{R,I}$ relations should be considered for the DE sample if the TF relation is to be evaluated as a distance tool.

From Table 4 it is clear that the R band yields the smallest scatter of 0.24 mag with a slope of -8.8 ± 0.4 for the DE sample when using H I line widths. It follows from Table 6 that, for an estimated $\sigma_{\rm depth} = 0.17$, the intrinsic scatter is most likely around 0.06 mag in the R band. This means that, ignoring any measurement error, distances can be determined with an accuracy of typically 3% if R-band luminosities and global H I profiles are employed and the above-mentioned corrections and selection criteria are applied. It seems somewhat unexpected that the near-infrared relation is a significantly worse distance estimator, providing a distance accuracy of only 10%. Note that both the R-band and K'-band relations have a similar tightness. The reason why the K'-band relation shows a larger scatter is its steeper slope.

9.2. *TF Constraining Galaxy Formation Scenarios: The $M^{b,i}_{B,R,I,K'}$–log $(2V_{\rm flat})$ Relations*

When using the TF relations to constrain galaxy formation scenarios, it is undesirable to apply selection criteria; one would like to examine a volume-limited sample yet pay attention to the meaning of the observables. In numerical simulations of galaxy formation one usually identifies the dark matter halos and measures their masses to determine the rotational velocity of the embedded stellar disk. However, it was demonstrated in § 4 that, observationally, the width of the global H I profile is not always a good measure of this rotational velocity induced by the mass of the dark matter halo, i.e., the amplitude of the outer flat part of the rotation curve. One should be extremely careful when selecting the appropriate samples and observables.

For example, Navarro & Steinmetz (2000) found that the results from their galaxy formation simulations are in agreement with the statistical properties of the H I sample. They appropriately rejected the observed statistical properties of the smaller DE sample given the notion that those galaxies are selected on the basis of their regular morphological appearance. However, although the H I sample is more complete, the line widths $W^i_{R,I}$ of many galaxies in the H I sample do not relate to $V_{\rm flat}$. For their purposes, Navarro & Steinmetz (2000) should have considered the statistical properties of the steeper and tighter $M^{b,i}_{K'}$–log $(2V_{\rm flat})$ correlation for the RC/$FD^{\rm NGC\,3992}$ sample; all galaxies should be considered in the entire volume-limited sample for which $V_{\rm flat}$ could actually be measured. The other galaxies in the UMa volume are strongly interacting, are too poor in H I, are too face-on, or have rising rotation curves for which $V_{\rm flat}$ could not be measured. Note that these galaxies were mainly rejected because of observational issues, not because of their intrinsic properties, except for the interacting systems for which $V_{\rm flat}$ cannot be related to the mass of the dark matter halo without knowing the dynamics of the interaction.

Examining the results from the inverse least-squares fits to the $M^{b,i}_{B,R,I,K'}$–log $(2V_{\rm flat})$ relations in Table 4 indicates, going from the blue to the near-infrared, a progressively steeper relation with a decreasing scatter and, above all, a decreasing $\chi^2_{\rm red}$. The corresponding estimated intrinsic scatters are 0.31, 0.15, 0.12, and 0.00 mag for the B, R, I, and K' bands, respectively, based on $\sigma_{\rm depth} = 0.17$. This implies that no intrinsic scatter is required to explain the observed scatter in the $M^{b,i}_{K'}$–log $(2V_{\rm flat})$ relation.

10. LOW SURFACE BRIGHTNESS GALAXIES AND THE TF RELATION

It was shown by Zwaan et al. (1995) that LSB and HSB galaxies of the same luminosity lie at the same location in the $M^{b,i}_B$–log $W^i_{R,I}$ TF relation, at least within the $\sim$0.8 mag scatter of their B-band relation. Since LSB galaxies tend to be bluer than their HSB counterparts of the same total mass, this situation must change with passband. If the assertion of Zwaan et al. (1995) is correct, one consequently would expect the LSB galaxies to be underluminous with respect to the HSB galaxies in the K'-band TF relation.

Figure 8 shows the $M^{b,i}_{B,K'}$–log $(2V_{\rm flat})$ relations for the RC/$FD^{\rm NGC\,3992}$ sample. The filled circles indicate the HSB galaxies, and the open circles correspond to the LSB systems. The distinction between HSB and LSB is made at the near-infrared central disk surface brightness of $\mu^i_0(K') = 18.5$ mag as motivated in Paper II. The sample of 21 galaxies in the RC/$FD^{\rm NGC\,3992}$ sample contains 13 HSB and eight LSB galaxies with average $B-K'$ colors of 3.28 ± 0.36 (scatter) and 2.52 ± 0.39 (scatter), respectively. This difference, or offset, of 0.76 mag should become evident when comparing the B-band and the K'-band relations.

Although HSB and LSB galaxies of similar luminosity can be found in the UMa sample, the surface brightness correlates rather strongly with total luminosity. In the current sample, the overlap region between HSB and LSB galaxies is limited (see Fig. 8), which complicates a direct comparison of the HSB and LSB subsamples. Nevertheless, panel (8a) of Figure 7 does show a significant correlation between the $M^{b,i}_B$–log $(2V_{\rm flat})$ residuals and the near-infrared central disk surface brightness. Such a correlation does not exist for the $M^{b,i}_{K'}$–log $(2V_{\rm flat})$ residuals (panel [8b]). Therefore, it should be concluded that the current UMa sample indicates that there does exist an offset between HSB and

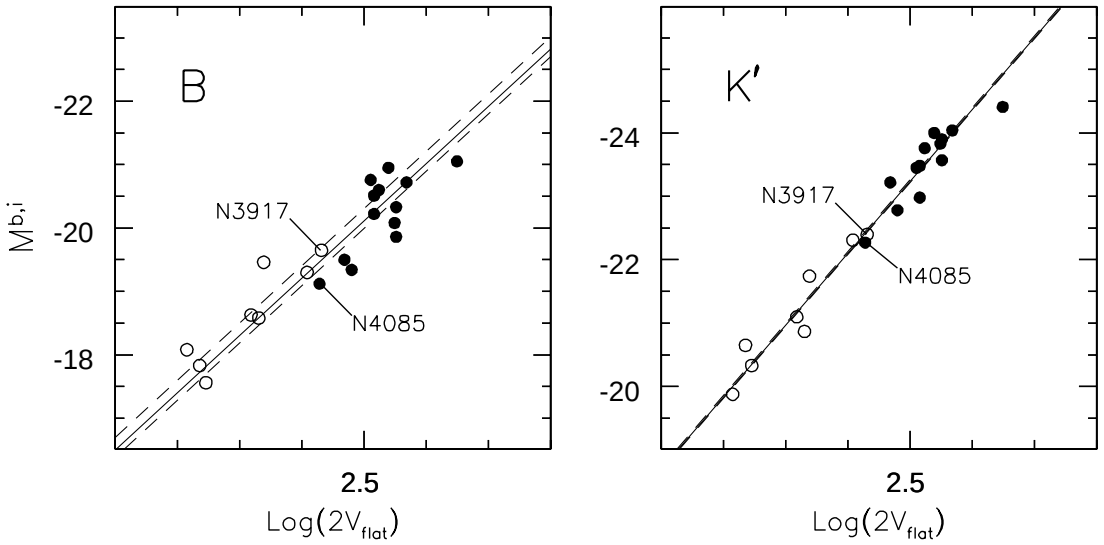

FIG. 8.—$M^{b,i}_{B,K'}$–log ($2V_{\rm flat}$) relations for the RC/$FD^{\rm NGC\ 3992}$ sample. In this case, the filled circles indicate the HSB galaxies, and the open circles correspond to the LSB systems. The solid lines correspond to inverse fits to all the galaxies. The dashed lines show the fits to the HSB and LSB subsamples separately, keeping their slopes fixed to those of the solid lines. The HSB/LSB galaxy pair NGC 3917/NGC 4085 discussed in the text is indicated.

LSB galaxies in the *B*-band TF relation in the sense that LSB galaxies are overluminous compared to HSB galaxies with similar $V_{\rm flat}$, or they rotate too slowly compared to their *B*-band equiluminous HSB counterparts. However, no such offset could be detected in the tighter near-infrared relation. This implies that the offset between HSB and LSB galaxies in the *B*-band TF relation is caused by differences in the mass-to-light ratios of their stellar populations. The offset is luminosity based and not mass related; LSB galaxies are indeed overluminous in the *B* band. The fact that no offset could be detected in the *K*′-band TF relation indicates that $V_{\rm flat}$ is unrelated to the gravitational potential of the stellar component.

It should be noted that the corrections for internal dust extinction complicate the situation in the *B* band somewhat since the applied corrections depend on total luminosity (or line widths), regardless of surface brightness; HSB and LSB galaxies of the same luminosity received the same extinction correction (see Paper IV). Observationally, however, LSB galaxies turn out to be virtually dust free. The LSB galaxies in the UMa sample are hardly detected by *IRAS*, and in general, no CO emission from LSB systems can be detected (de Blok & van der Hulst 1998). This is illustrated by the HSB/LSB galaxy pair NGC 4085/NGC 3917 for which the relevant data are listed in Table 7. These two galaxies are of similar morphological type and mass ($V_{\rm flat}$) but of different surface brightness. Note that the observed color $m^b_B - m^b_{K'}$ (uncorrected for internal extinction) of the HSB galaxy NGC 4085 is somewhat redder (3.85) than that of the LSB galaxy (3.50). Most importantly, the relative far-infrared luminosity of the HSB galaxy is 6–7 times higher than that of the LSB system, indicating that the HSB galaxy is much dustier than the LSB system. Note also that the dust in the LSB galaxy is colder than that in the HSB system, which still leaves the possibility that large amounts of undetected obscuring colder dust may be present in NGC 3917.

11. THE BARYONIC TF RELATION

The tightest correlation, with a slope of $b = -11.3$, is found between the *K*′ luminosity of a galaxy and $V_{\rm flat}$, the rotational velocity induced by the dark matter halo. Since the *K*′ light is thought to be a good tracer of the stellar mass, one may wonder whether the near-infrared TF relation changes significantly if the total baryonic mass, i.e., stars plus gas, is considered instead of just the stellar mass. This issue has been previously explored by McGaugh et al. (2000), who noted a break in the TF relation around $0.5W^i_{R,I} = 90$ km s^{-1} below which galaxies are underluminous. They were able to restore a linear TF relation by taking the gas mass of the galaxies into account. This break in the TF relation is not evident in the current UMa sample because it lacks galaxies with $V_{\rm flat} < 80$ km s^{-1}. Nevertheless, the available UMa data are accurate enough to expect significant differences between a luminosity-based and a mass-based TF relation for galaxies with $V_{\rm flat} > 80$ km s^{-1}.

To study this issue with the current sample, a baryonic luminosity is calculated for all the galaxies by converting their gas content (H I + He) into stellar *K*′ light according

TABLE 7

VARIOUS PROPERTIES OF THE HSB/LSB PAIR NGC 3917 AND NGC 4085

Name	Type	$\mu^i_0(K')$ (mag arcsec^{-1})	$V_{\rm flat}$ (km s^{-1})	$M^{b,i}_B$ (mag)	$M^{b,i}_{K'}$ (mag)	$\Delta M^{b,i}_B$ (mag)	$\Delta M^{b,i}_{K'}$ (mag)	A^i_B (mag)	$A^i_{K'}$ (mag)	M^b_B (mag)	$M^b_{K'}$ (mag)	$F_{60\,\mu m}$ (Jy)	$F_{100\,\mu m}$ (Jy)	$L_{\rm FIR}$ ($10^9 L_\odot$)	$L_{\rm FIR}/L^b_B$	$L_{\rm FIR}/L^b_{K'}$
NGC 3917...	Scd	18.66	135±3	−19.65	−22.40	0.23	0.05	0.87	0.12	−18.78	−22.28	0.61±0.05	3.16±0.22	0.64	0.13	0.04
NGC 4085...	Sc	17.36	134±6	−19.12	−22.27	−0.27	−0.05	0.78	0.11	−18.34	−22.16	5.49±0.27	14.61±0.73	3.91	1.18	0.25

TABLE 8

STATISTICAL PROPERTIES OF THE BARYONIC TF RELATION FOR VARIOUS VALUES OF THE MASS-TO-LIGHT RATIO OF THE GAS

$(M_{gas}/L_{K'})$	Zero Point (mag)	Slope	rms (mag)	χ^2_{red}	Q
0.1.....	−5.63	−7.4	0.53	9.2	0.00
0.2.....	−4.38	−7.8	0.41	5.1	0.00
0.4.....	−2.36	−8.5	0.33	2.9	0.00
0.8.....	−0.17	−9.3	0.28	1.7	0.02
1.6.....	1.66	−10.0	0.25	1.2	0.17
3.2.....	3.07	−10.5	0.24	1.1	0.33
6.4.....	3.93	−10.9	0.25	1.0	0.38
12.8	4.47	−11.1	0.25	1.0	0.37

NOTE.—It is assumed that $\sigma^2_{depth} + \sigma^2_{intr} = 0$.

to $L_{K',gas} = 1.4\mathcal{M}_{H\,I}/(\mathcal{M}_{gas}/L_{K'})$. The factor 1.4 accounts for the helium mass fraction, while the dust mass is neglected. This K' luminosity of the gas is then added to the extinction-corrected stellar luminosity to yield a baryonic luminosity, $L^{b,i}_{bar} = L^{b,i}_{K',stars} + L_{K',gas}$.

Because the fainter galaxies are relatively more gas-rich (see Fig. 5 of Paper IV), $L_{K',gas}$ will add relatively more to the stellar luminosity of the fainter galaxies, and consequently the slope of the baryonic TF relation will become shallower than the $b = -11.3$ of the K' luminosity–based TF relation. However, it is not guaranteed that the tightness of the K' luminosity–based TF relation will be maintained. Results from the inverse least-squares fits to the baryonic $L_{K',bar}$–log $(2V_{flat})$ correlation are given in Table 8 for a range of values for $(\mathcal{M}_{gas}/L_{K'})$.

As can be seen from Table 8, a slope of $b = -10.0$ is found when $(\mathcal{M}_{gas}/L_{K'}) = 1.6$ is assumed (see also Fig. 9). Furthermore, it follows that the 95% confidence interval for $(\sigma^2_{depth} + \sigma^2_{intr})^{1/2}$ is (0.00–0.14–0.27). Consequently, in the case $\sigma_{depth} = 0.17$, there is most likely no intrinsic scatter. In conclusion, the slope of $b = -11.3$ that is found for the tightest luminosity-based TF relation, the near-infrared $M^{b,i}_{K'}$–log $(2V_{flat})$ correlation, is reduced to $b = -10.0$ if the gaseous component is converted into starlight on the basis of $(\mathcal{M}_{gas}/L_{K'}) = 1.6$ in which case a zero intrinsic scatter remains most likely.

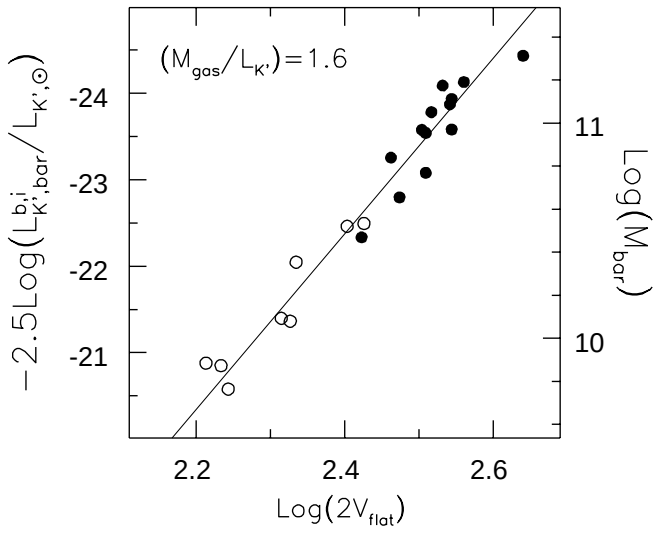

FIG. 9.—Baryonic log $\mathcal{M}_{bar}$–log $(2V_{flat})$ TF relation for the RC/$FD^{NGC\,3992}$ sample assuming a mass-to-light ratio of 1.6 for the gas. The solid symbols indicate HSB galaxies, open symbols indicate LSB systems. The solid line shows an inverse least-squares fit to all the points and has a slope of −10.0.

12. DISCUSSION

This study is the first one that considers a complete volume-limited cluster sample of galaxies for which H I velocity fields are obtained as well as multiband optical and near-infrared imaging photometry. As such, the UMa data set is unique, but nevertheless, the current results should be compared to at least a few of many other studies that relate the shape of the rotation curves to the statistical properties of the TF relation. These studies come in several flavors, depending on how the rotation curves are measured, either via H I synthesis observations or by means of optical spectroscopy and either with long-slit spectroscopy (or its radio equivalent) along the major axis or through observations of a galaxy's full velocity field. Each methodology has its limitations in the extent of the interpretation of the data, However, it is most important to keep in mind that optical measures of a galaxy's rotation are always limited to the inner regions of a (star-forming) stellar disk, no matter which method is employed. Optical observations cannot probe a galaxy's rotation in the outer regions beyond the detectable stellar disk where the gravitational potential is dominated by the dark matter halo. This realm can only be probed accurately by studying the kinematics of the extended H I disk.

Broeils (1992) collected accurate H I rotation curves from the literature for a sample of 21 field galaxies with H I velocity fields. About half of these galaxies show a significantly declining part. Using B-band magnitudes, he found scatters of 0.70 mag when using global profile widths, 0.62 mag when using V_{max}, and 0.55 mag when using V_{flat} with slopes of −7.4, −8.3, and −8.5, respectively. The correction methods he applied are somewhat different from the ones applied to the UMa data used in this paper (see Paper IV for an extensive comparison and discussion), and, unfortunately, it is not clear which fitting method, direct or inverse, he applied. Although he found much larger scatters than are found for the current UMa sample (he used a nearby field sample with significant distance uncertainties), he found the same trends in the scatter and slope of the relation. In the current case, however, nearly identical slopes are found when using W^i_R and V_{max}, thanks to a more appropriate value for the turbulent motion parameter W_t (see Paper IV). Broeils (1992) also made short WSRT observations (nearly equivalent to optical long-slit spectroscopy) of a sample of 48 nearby field galaxies. In this larger sample he did not identify galaxies with rising, flat, or declining rotation curves but merely measured a "representative" rotational velocity and subsequently found no improvement in the TF relation when using this velocity instead of the global profile width; the observed scatters were 0.77 and 0.81 mag with slopes of −6.6 and −6.3, respectively. His conclusion that a reduction of the scatter can only be achieved with more information about the inclination angle to be derived from full H I velocity fields was an important motivation for the current UMa study.

Several years later, Rhee (1996) supplemented the two samples of Broeils, who in the meantime had measured seven more rotation curves derived from full velocity fields.

Rhee himself analyzed short WSRT observations of 60 more spirals. With these larger samples of 28 velocity fields and 108 short observations, Rhee (1996) reached exactly the same conclusions as Broeils (1992) did before: rotation curves derived from "long-slit" H I observations are not helpful to reduce the scatter as a result of a lack of information about the inclination of a galaxy. This inclination angle and its possible change with radius can be retrieved from an H I velocity field, however, and that is why they advocate the use of full galactic velocity fields for deriving accurately the rotational velocity of a galaxy.

The investigations by Broeils and Rhee are the only ones so far that exploit the advantages of H I synthesis observations in an attempt to gain a better understanding of the statistical properties of the TF relation. This is mainly because the reduction and interpretation of H I synthesis data are very elaborate. And indeed, studies using optical observations occur more frequently. The major advantage of optical spectroscopy is the much higher spatial resolution of the data compared to that of radio synthesis data. The disadvantages of optical spectroscopy, however, are the relatively low velocity resolution, the limited radial coverage, and the influence of obscuring dust in the observed galaxies. Nevertheless, many investigators used Hα long-slit spectroscopy to retrieve the rotation curve of a galaxy (e.g., Rubin et al. 1985; Courteau 1992; Mathewson, Ford, & Buchhorn 1992; Vogt et al. 1997; Raychaudhury et al. 1997; Willick 1999 and many references therein).

Rubin et al. (1985) noted a morphological segregation in the B- and H-band TF relations constructed by using $V_{\max}$ from their optical rotation curves. They constructed separate TF relations for Sa-, Sb-, and Sc-type spirals selected from the nearby field and noted that, although the slopes are similar for each morphological class, in the B band, earlier type spirals are offset toward higher rotational velocities with respect to later type spirals. This offset is less but not zero when using H-band magnitudes. Their rotation curves do not reach beyond R_{25}, and a decline in the rotation curve beyond this radius, as is seen in the case of NGC 3992 (see Fig. 2), would not have been detected by them. They did not have the possibility to explore the shapes of the rotation curves in the outer regions. Furthermore, they found rather large scatters of 0.7 mag in both passbands after shifting the three separate relations, one for each morphological bin, on top of each other. These results of Rubin et al. (1985) can be reconciled with the current findings by noting that declining rotation curves are mainly found in early-type spirals. It was impossible for Rubin et al. (1985) to measure the rotation curve at large enough distances from the center to reveal a significantly declining part in the outer regions. Apparently, in most cases, the relevant kinematic information is found in the very outer parts of the rotation curves, beyond R_{25}.

Recently, Raychaudhury et al. (1997) investigated the I-band TF relation for a sample of spirals in the Coma Cluster using long-slit Hα spectroscopy. They found, for a sample of 25 carefully selected Sb–Sd spirals, an unusually shallow slope of -5 and a remarkably low scatter of only 0.14 mag, barely consistent with their observational uncertainties. They investigated whether the scatter could be reduced even further by using the shape of the rotation curve as an extra parameter. They quantified the shape in terms of the steepness of the rotation curve in the inner part and, not surprisingly, failed to reduce the scatter any further. As a result of a lack of signal, they were not able to measure the shape of the rotation curve in the outer regions.

Schommer et al. (1993) present an extensive study using Fabry-Perot techniques to map the Hα velocity fields of 75 spirals in three clusters. By fitting tilted rings to the velocity fields, they derive rotation curves from which they extract the circular velocity. A comparison of these circular velocities with the velocities derived from global H I profiles shows that the Hα velocities are often estimated too low. It can be noted from their published rotation curves that many are still rising at their last measured points, and for those cases it is likely that a more extended H I disk would show a significantly faster rotation in the outer regions. Unfortunately, they did not check whether the deviations between the optically and H I derived rotational velocities are related to the slope of the optical rotation curves at the last measured points. Anyway, using I-band magnitudes, they constructed TF relations for seven galaxies in the Antlia Cluster and 10 galaxies in the Hydra Cluster. From double regression fits, they find scatters of 0.18 and 0.29 mag for the two clusters with slopes of -8.8 ± 0.8 and -9.8 ± 0.8, respectively.

Reviewing these studies of the TF relation, which make use of available rotation curves, illustrates that measuring rotation curves via optical spectroscopy gives insufficient information about the shape of rotation curves in the relevant outer regions of spirals.

The two main applications of the TF relation are measuring galaxy distances and constraining galaxy formation scenarios. These applications require different approaches for constructing the samples (only Sc vs. all types), collecting the data (global profiles vs. rotation curves), retrieving the appropriate measures from the data ($V_{\max}$ vs. $V_{\rm flat}$), and interpreting the results in relation to their applications (scatter vs. tightness). Without sufficient information about the shapes of galaxy rotation curves, it becomes difficult to reliably relate the observed scatter in the TF relation to, for instance, the results of numerical galaxy formation simulations. The main problem is that the rotational velocity of a galaxy is simply not well defined. The rotational velocity induced by the dark matter halo ($V_{\rm flat}$) in the outer parts of a galaxy often cannot be retrieved from global profiles or optical and even H I rotation curves, no matter how accurate the observable is determined. This is especially the case for volume-limited samples that contain a wide range of galaxy morphologies and gas mass fractions.

Using the TF relation as a distance estimator for large samples of galaxies requires the use of global H I profiles that can be collected efficiently with single-dish telescopes. The current UMa sample confirms that invoking strict selection criteria significantly reduces the scatter in the relation (H I sample vs. DE sample). Furthermore, the smallest rms scatter is obtained when using the global profile widths in conjunction with the R-band luminosities. The total observed scatter of 0.24 mag in the R band includes contributions from measurement uncertainties, the depth of the sample, and any "intrinsic" scatter. Removing the estimated contribution due to the depth of the sample (0.17 mag) and assuming that the measurement errors are typical for other observational surveys (0.05 mag in m_R and 5% in $W^i_{R,I}$) suggests that galaxy distances can be measured with a typical accuracy of about 7%.

When using the TF relation to constrain galaxy formation scenarios, one should consider the tightness of the rela-

tion and not so much the scatter along the magnitude axis. In this case one should also include the widest possible range of galaxy morphologies. Furthermore, making the observations compatible with the results from numerical simulations requires the measurement of $V_{\rm flat}$. Considering all UMa Cluster galaxies for which $V_{\rm flat}$ could be measured shows that the tightest correlation is found when using near-infrared K' luminosities ($N = 21$, $b = -11.3$, $\sigma_{\rm obs} = 0.26$ mag, $\chi^2_{\rm red} = 1.1$, excluding NGC 3992) with a most likely zero intrinsic scatter and a maximum allowed intrinsic scatter of 0.21 mag. The fact that the tightest correlation is found when using K' luminosities suggests that possibly the baryonic content of the dark matter halo is fundamentally related to the mass of the dark matter halo instead of the luminosity of the stellar component. After all, the K' luminosity is more closely related to the stellar mass than the optical luminosities are. In the previous section it was shown that the gaseous component can be converted into a K' luminosity that can be added to the stellar K' luminosity without losing the tightness of the correlation. It does, however, result in a shallower slope since the low-luminosity spirals are overall more gas-rich. A slope of -10 results when assuming a mass-to-light ratio of $(\mathscr{M}/L_{K'}) = 1.6$ for the stellar or gaseous component.

All these considerations suggest that the TF relation is fundamentally a correlation between the mass of the dark matter halo, expressed by $V_{\rm flat}$, and the total baryonic mass in that halo, while dark matter halos of the same mass are required to have an identical $V_{\rm flat}$. The fact that HSB and LSB galaxies follow the same near-infrared correlation and that the correlation based on $V_{\rm flat}$ is tighter than the correlation based on $V_{\rm max}$ indicates that the actual distribution of the baryonic mass inside the halo is irrelevant. Furthermore, for a reasonable mass-to-light ratio of the gas, the correlation between dark halo mass and baryonic mass has a slope of -10 with little room for any intrinsic scatter. The slopes of the luminosity-based TF relations and the scatter in the correlation in the optical passbands depend on the star formation histories and the resulting current stellar populations. The scatter in the B-band relation cannot entirely be interpreted in terms of noncircular motions, triaxial halo potentials, or other dynamical processes since the near-infrared correlation is significantly tighter. It should be recalled that these statements only apply to galaxies more massive than about twice the Small Magelanic Cloud.

13. SUMMARY

This study investigated the statistical properties of the TF relations for a complete volume-limited sample of galaxies in the nearby UMa Cluster. Total luminosities in the optical B, R, I, and near-infrared K' passbands were used in conjunction with the corrected global H I profile widths $W^i_{R,I}$ and information on the shapes of the H I rotation curves. The two most commonly used methods to correct the observed luminosity for internal extinction by dust are compared. Rising, flat, and declining rotation curves could be identified from which $V_{\rm max}$ and $V_{\rm flat}$ could be measured and related to $W^i_{R,I}$. The four luminosity and three kinematic measures allowed the construction of 12 TF correlations. The statistical properties of these 12 correlations were investigated for various subsamples that were constructed on the basis of the kinematic states of the galaxies and the practical applications of the correlation. Inverse least-squares fits were made taking fiducial errors in both directions into account.

When using the TF correlation as a distance estimator, the global profile widths $W^i_{R,I}$ and the R-band luminosities are the preferred observables in conjunction with strict selection criteria on the basis of overall morphology. The resulting correlation allows distance determinations with an accuracy of about 7%, taking typical measurement errors into account. This is based on a subsample of 16 critically selected galaxies.

Dropping the selection criteria and considering the correlations for larger subsamples using $W^i_{R,I}$ or $V_{\rm max}$ showed that galaxies with rising rotation curves lie on the low-velocity side of the correlation while galaxies with declining rotation curves tend to be offset to the high-velocity side. The subsample of galaxies with classical flat rotation curves shows a steeper and tighter correlation. When using $V_{\rm flat}$ instead of $W^i_{R,I}$ or $V_{\rm max}$, the offset for galaxies with declining rotation curves disappears. The tightest correlation is found when using K' luminosities and the amplitude $V_{\rm flat}$ of the flat part of the rotation curve. The tightness of this $M^{b,i}_{K'}$–log $(2V_{\rm flat})$ correlation, with a slope of -11.3, suggests a most likely intrinsic scatter of zero and an upper limit to the intrinsic scatter of 0.21 mag at the 95% confidence level. The residuals in the less tight blue $M^{b,i}_{B}$–log $(2V_{\rm flat})$ relation correlate with global properties along the Hubble sequence. Positive residuals are found for bluer spirals of lower surface brightness and later morphological type that have a relatively larger gas mass fraction. Notably, in the blue passband, LSB galaxies do not follow the same correlation as HSB galaxies since the residuals in the $M^{b,i}_{B}$–log $(2V_{\rm flat})$ relation do correlate with the central disk surface brightness. However, these correlations of the residuals with properties along the Hubble sequence disappear in the near-infrared.

A baryonic TF relation using $V_{\rm flat}$ is considered by converting the gas reservoir of a galaxy into a K' luminosity, assuming a range of values for $(M_{\rm gas}/L_{K'})$, and adding that to the stellar K' luminosity. A slope of -10.0 is found in the case $(\mathscr{M}_{gas}/L_{K'}) = 1.6$, while the tightness of the correlation is maintained with a most likely intrinsic scatter of zero for the baryonic TF relation.

These findings indicate that the TF relation is fundamentally a correlation between the maximum rotational velocity of the dark matter halo ($V_{\rm flat}$) and the total baryonic mass inside that halo. The actual distribution of the baryonic mass inside the dark matter halo is irrelevant. The scatter in the optical passbands is mainly related to varying star formation histories and internal dust extinctions.

I wish to thank Renzo Sancisi and Brent Tully for initiating the UMa Cluster project and for their collaborative support. Much of this work was carried out at the Kapteyn Institute in Groningen, the Institute for Astronomy in Honolulu, and the National Radio Astronomy Observatory in Socorro. The Westerbork Synthesis Radio Telescope is operated by the Netherlands Foundation for Research in Astronomy (NFRA) with financial support from the Netherlands Organization for Scientific Research (NWO). This research has been supported by the Leids Kerkhoven-Bosscha Fonds, NATO collaborative research grant 940271, and the National Science Foundation grant AST-9970780.

REFERENCES

Beers, T. C., Flynn, K., & Gebhardt, K. 1990, AJ, 100, 32
Bell, E. F., & de Jong, R. S. 2001, ApJ, 550, 212
Bernstein, G. M., Guhathakurta, P., & Raychaudhury, S. 1996, in Proc. of the ESO/MPA Workshop, Spiral Galaxies in the Near-IR, ed. D. Minniti & H.-W. Rix (Berlin: Springer), 200
Bernstein, G. M., Guhathakurta, P., Raychaudhury, S., Giovanelli, R., Haynes, M. P., Herter, T., & Vogt, N. P. 1994, AJ, 107, 1962
Broeils, A. H. 1992, in Dark and Visible Matter in Spiral Galaxies (Groningen: Rijksuniversiteit Groningen), chap. 3
Bullock, J. S., Kolatt, T. S., Sigad, Y., Somerville, R. S., Kravtsov, A. V., Klypin, A. A., Primack, J. R., & Dekel, A. 2001, MNRAS, 321, 559
Casertano, S., & van Gorkom, J. H. 1991, AJ, 101, 1231
Condon, J. J., Cotton, W. D., Greisen, E. W., Yin, Q. F., Perley, R. A., Taylor, G. B., & Broderick, J. J. 1998, AJ, 115, 1693
Courteau, S. 1992, Tully-Fisher Distances and Motions in the Northern Sky (Santa Cruz: Univ. California)
Courteau, S., & Rix, H.-W. 1999, ApJ, 513, 561
Davis, M., & Peebles, P. J. E. 1983, ARA&A, 21, 109
de Blok, W. J. G., & van der Hulst, J. M. 1998, A&A, 336, 49
di Nella, H., Garcia, A. M., Garnier, R., & Paturel, G. 1995, A&AS, 113, 151
Falco, E. E., et al. 1999, PASP, 111, 438
Fisher, J. R., & Tully, R. B. 1981, ApJS, 47, 139
Franx, M., & de Zeeuw, P. T. 1992, ApJ, 392, L47
Freedman, W. L. 1990, ApJ, 355, L35
Giovanelli, R., Haynes, M. P., Herter, T., Vogt, N. P., da Costa, L. N., Freudling, W., Salzer, J. J., & Wegner, G. 1997, AJ, 113, 53
Giovanelli, R., Haynes, M. P., Salzer, J. J., Wegner, G., da Costa, L. N., & Freudling, W. 1994, AJ, 107, 2036
Hinz, J. L., Rix, H.-W., & Bernstein, G. M. 2001, AJ, 121, 683
Kraan-Korteweg, R. C., Cameron, L. M., & Tammann, G. A. 1988, ApJ, 331, 620
Malhotra, S., Spergel, D. N., Rhoads, J. E., & Li, J. 1996, ApJ, 473, 687
Mathewson, D. S., Ford, V. L., & Buchhorn, M. 1992, ApJS, 81, 413
McGaugh, S. S., Schombert, J. M., Bothun, G. D., & de Blok, W. J. G. 2000, ApJ, 533, L99
Navarro, J. F., & Steinmetz, M. 2000, ApJ, 538, 477
Peletier, R. F., & Willner, S. P. 1993, ApJ, 418, 626
Pierce, M. J., & Tully, R. B. 1988, ApJ, 330, 579
Raychaudhury, S., von Braun, K., Bernstein, G. M., & Guhathakurta, P. 1997, AJ, 113, 2046
Rhee, M.-H. 1996, A Physical Basis of the Tully-Fisher Relation (Zoetermeer: Park Publishing)
Rix, H.-W., Guhathakurta, P., Colless, M., & Ing, K. 1997, MNRAS, 285, 779
Rubin, V. C., Burstein, D., Ford, W. K., Jr., & Thonnard, N. 1985, ApJ, 289, 81
Sakai, S., et al. 2000, ApJ, 529, 698
Schommer, R. A., Bothun, G. D., Williams, T. B., & Mould, J. R. 1993, AJ, 105, 97
Trentham, N., Tully, R. B., & Verheijen, M. A. W. 2001, MNRAS, 325, 385 (Paper III)
Tully, R. B., & Fisher, J. R. 1977, A&A, 54, 661
Tully, R. B., & Fouqué, P. 1985, ApJS, 58, 67 (TF85)
Tully, R. B., & Pierce, M. J. 2000, ApJ, 533, 744
Tully, R. B., Pierce, M. J., Huang, J.-S., Saunders, W., Verheijen, M. A. W., & Witchalls, P. L. 1998, AJ, 115, 2264
Tully, R. B., & Verheijen, M. A. W. 1997, ApJ, 484, 145 (Paper II)
Tully, R. B., Verheijen, M. A. W., Pierce, M. J., Huang, J.-S., & Wainscoat, R. J. 1996, AJ, 112, 2471 (Paper I)
van Albada, T. S., & Sancisi, R. 1986, Philos. Trans. R. Soc. London A, 320, 447
Verheijen, M. A. W., & Sancisi, R. 2001, A&A, 370, 765 (Paper IV)
Vogt, N. P., et al. 1997, ApJ, 479, L121
Willick, J. A. 1999, ApJ, 516, 47
Zwaan, M. A., van der Hulst, J. M., de Blok, W. J. G., & McGaugh, S. S. 1995, MNRAS, 273, L35